

## Article

# Performance Signature of the Best Candidate-Graded Bandgap Materials for Solar Cells with Steady-State Conversion Efficiency

Hazem M. El-Hageen <sup>1,2,3,\*</sup> , Ahmed Nabih Zaki Rashed <sup>4</sup> , Hani Albalawi <sup>1,2</sup>, Mohammed A. Alhartomi <sup>1</sup> , Yousef H. Alfaifi <sup>5</sup>, Madhi Tarikham Alsubaie <sup>1</sup> and Mohamed A. Mead <sup>6</sup>

<sup>1</sup> Electrical Engineering Department, Faculty of Engineering, University of Tabuk, Tabuk 47913, Saudi Arabia; halbala@ut.edu.sa (H.A.); malhartomi@ut.edu.sa (M.A.A.); 391003657@stu.ut.edu.sa (M.T.A.)

<sup>2</sup> Renewable Energy and Energy Efficiency Center (REEEC), University of Tabuk, Tabuk 47913, Saudi Arabia

<sup>3</sup> Egyptian Atomic Energy Authority, Cairo 13759, Egypt

<sup>4</sup> Electronics and Electrical Communications Engineering Department, Faculty of Electronic Engineering, Menoufia University, Menouf 32951, Egypt; ahmed\_733@yahoo.com

<sup>5</sup> Faculty of Computers and Information Technology, University of Tabuk, Tabuk 47913, Saudi Arabia; y\_alfaifi@ut.edu.sa

<sup>6</sup> Faculty of Computers and Informatics, Suez Canal University, Ismalia 41522, Egypt; mohamedmead@ci.suez.edu.eg

\* Correspondence: helhageen@ut.edu.sa or hazemhageen@hotmail.com

**Abstract:** This is a comprehensive research endeavor focused on enhancing the efficiency of the proposed solar cell design. The integration of the simulation techniques, judicious material selection, and meticulous performance metrics showcase a methodical approach toward creating a solar cell capable of achieving high efficiency across a wide spectrum of light in the AM 1.5 G1 sun solar cell illumination spectrum. Having said this, many researchers are still working on the efficiency potential—based on external radiative efficiency (ERE), open-circuit voltage loss, and fill factor loss—of high-efficiency solar cells. The solar cell is built on aluminum-doped zinc oxide (ZnO) as a transparent conductive oxide layer; aluminum nitride (AlN) as the window layer (emitter); an SWCNT layer as the absorber layer; gallium phosphide (GaP) as the contact layer; and silicon as the substrate. The proposed solar cell transmission, reflection, and absorption relative to the variations in wavelength band spectrum are studied. The conduction and valence band energy diagrams of the solar cell design structure are simulated against the layer thickness variations for the suggested solar cell structure. Short-circuit current density and maximum power variations are clarified versus the bias voltage. Light current density is simulated versus the bias voltage ( $J/V$  characteristics curve) of the suggested solar cell design structure. The carrier generation–recombination rate is also simulated by the COMSOL simulation program versus the layer thickness of the suggested solar cell structure. The solar cell circuit design has a fill factor ( $FF$ ) value of 74.31% and a power conversion efficiency value of 29.91%.

**Keywords:** optimum absorber layer; solar cell structure; surface morphology; conversion efficiency and quantum efficiency



**Citation:** El-Hageen, H.M.; Zaki Rashed, A.N.; Albalawi, H.; Alhartomi, M.A.; Alfaifi, Y.H.; Alsubaie, M.T.; Mead, M.A. Performance Signature of the Best Candidate-Graded Bandgap Materials for Solar Cells with Steady-State Conversion Efficiency. *Energies* **2023**, *16*, 7001. <https://doi.org/10.3390/en16197001>

Academic Editor: Sungjin Jo

Received: 12 August 2023

Revised: 12 September 2023

Accepted: 17 September 2023

Published: 9 October 2023



**Copyright:** © 2023 by the authors. Licensee MDPI, Basel, Switzerland. This article is an open access article distributed under the terms and conditions of the Creative Commons Attribution (CC BY) license (<https://creativecommons.org/licenses/by/4.0/>).

## 1. Introduction

The most significant and environmentally beneficial source of renewable energy is solar energy; it is free, abundantly available, and widely applicable everywhere on Earth. Therefore, the expected demand for solar energy is constantly increasing, along with efforts to increase its production efficiency. The development of technologies, materials, internal structure, design, and other factors have been studied with the aim of increasing the steady-state conversion efficiency of solar cells. One of the most important means for this purpose is the introduction of metal nanoparticles. The silicon-based solar cell's absorption coefficient can be raised by creating a heterojunction, which enhances its efficiency [1].

A platinum precursor solution was designed to fabricate the active counter electrodes suitable for efficient dye-sensitized solar cells. The solar cell assembly was built with six different concentrations. The measurements of light voltage curves were tested, and the electrochemical impedance was measured at a standard of AM 1.5 G solar light. Simulated photo-voltage and photo-current density variations were found. The proposed solar cells' electrochemical impedance parameters were used to evaluate the fill factor, as well as the overall efficiency [2].

The graded energy band gap is a powerful method for increasing the effectiveness of the sun spectrum by reducing the losses in short-circuit current density [3]. Perovskite solar cells are one of the most promising technologies in this field. The efficiency of the suggested graded  $\text{FAPbI}_3$  perovskite solar cell was investigated together with the impact of (Br, I). The graded energy band gap perovskite solar cell can achieve steady-state conversion efficiencies of  $\sim 26.63\%$ . Another bandgap grading (1–3 eV) profile was proposed to maximize the perovskite absorber material's ability to absorb the spectrum. The bandgap of the Pb-based  $\text{MAPbX}_3$  was 2 eV, while that of the Sn-based  $\text{MASnX}_3$  was 1.17 eV, which is used in this design. A 1D Solar Cell Capacitance Simulator (SCAPS-1D) was used to simulate the current density (J)–voltage (V), capacitance (C)–voltage (V), and capacitance (C)–frequency (f) curves; the quantum efficiency curves; band diagrams; and the recombination current. Their proposed design has a 30% power conversion efficiency [4]. A certain study used the SCAPS-1D software, version 3.3.05 package to prove that, compared to a CdTe cell, the performance of a four-terminal (4T) perovskite–CdTe tandem is more efficient [5]. The numerical modeling of fluorine-doped tin oxide (FTO)/Cu:NiO/ $\text{MA}_3\text{Sb}_2\text{I}_9$ /ZnO/Al, which was based on perovskite solar cells by SCAPS, produced a power conversion efficiency (PCE) of 22.03% [6]. Regarding the photoelectric characteristics of ZnO/Si and perovskite/Si, the impacts of the gold nanoparticles of various sizes and periodicities were studied. The results showed that the maximum values of the fill factor, open-circuit voltage, and short-circuit current were 71.06%, 0.384 V, and 10.47  $\text{mA}/\text{cm}^2$  for perovskite/Si, as well as 71.12%, 0.306 V, and 10.52  $\text{mA}/\text{cm}^2$  for ZnO/Si [7]. The study presented  $\text{CH}_3\text{NH}_3\text{PbI}_{3-x}\text{Cl}_x$  perovskite solar cells beside the light detection conducted with the SCAPS simulation program [8]. The authors studied the effects of the front/back electrode on the performance parameters of the solar cell design. The authors confirmed that a 22.7% max. conversion power efficiency with an open-circuit voltage of 1130 mV could be achieved with the optimization of the solar cell device performance parameters.

A zinc oxide/silicon (ZnO/Si) heterojunction has recently been used in the manufacturing of solar cells because of their potentially low-cost application. The authors optimized the design and performance properties of the ZnO/p-Si solar cell-based heterojunction structure with the SCAPS-1D Simulator. The effects of the defects at the ZnO/c-Si heterojunction interface were investigated. The study confirmed that the solar cell device performance efficiency achieved optimum values by using the optimum thin buffer layer. By effectively controlling the interface  $D_{it}$  and silicon layer defects, the ZnO/c-Si heterojunction solar cells' conversion efficiency showed the potential to be raised above 17%. The effects of emitter layer thickness, buffer layer thickness, interface defect states, and emitter and absorber defect density on cell performance were studied and analyzed, and the simulation results were thusly presented. The results show that a cell with an optimum thin buffer layer performs better. Also, the performance of the solar cells was significantly more sensitive to the defects in the Si than in the ZnO layer [9]. The authors paid attention to analyzing the solar cells' front side. An antireflective coating and amorphous silicon oxide layer were used with three front contact stacks: indium tin oxide (ITO) as a reference; ZnO:Al and ZnO:Al/SiO<sub>2</sub> in their design. The simulations and experimental results of this design yielded maximum conversion efficiencies of 23.0% [10]. A wide-gap n-type doped ZnO layer acting as a front electron-selective contact layer on a single-junction GaAs substrate was proposed to block hole transport and promote electron collection at the front side. By simulation, the authors showed that depositing a wide-gap ZnO window

layer enhances cell absorption in the short wavelength range, and it can be used in highly efficient single-junction GaAs cells [11].

Sb<sub>2</sub>Se<sub>3</sub>'s thin-film crystallinity has been extensively exploited as an absorber layer in solar cells. Several studies have used SCAPS-1D to complete simulation work based on Sb<sub>2</sub>Se<sub>3</sub>/c-Si hetero-junction solar cells [12–14]. The simulation included its band gap, thickness of layers, absorption coefficient, and the extraction of parameters, such as back contact work function and electron affinity (which were varied and optimized to improve the solar cell's performance). Also, parameters such as short-circuit current density ( $J_{sc}$ ), open-circuit voltage ( $V_{oc}$ ), quantum efficiency (QE), fill factor (FF), and the efficiency of the devices were examined graphically. The maximum efficiency reached 23.9% under the condition of an illumination spectrum of AM 1.5 G. SCAPS was used to study an extremely resistant transparent oxide material for usage as a solar cell's front contact. The optical and photoelectric characteristics of the solar cell, based on the heterostructure ZnO/CdS/CdTe/CuO, were modeled to study the influence of film thickness on the performance efficiency, which was recorded as 20.94% in this study [15].

There are other programs that were used to simulate a solar cell and to investigate its characteristics and performance. Through electromagnetic waves, semiconductors, and heat transfer modules, COMSOL is able to compute the optical–electrical–thermal models for a finely meshed structure. A COMSOL multiphysics 3-D simulation investigation of the optical, electrical, and thermal properties of a Cu<sub>2</sub>ZnSnS<sub>x</sub>Se<sub>4-x</sub> (CZTSSe) thin-film solar cell has been reported in many works [16,17]. COMSOL is used for the purpose of analyzing the temperature distribution in typical perovskite solar cells [18,19]. The performance of CH<sub>3</sub>NH<sub>3</sub>PbI<sub>3</sub> absorber thickness and the addition of pyramid grating to electron transporting layers was studied by COMSOL, and this caused the power conversion efficiency to rise to 21.058% [19]. In many articles [20–23] on the design of solar cells and their corresponding performance parameters—such as  $V_{OC}$ ,  $J_{sc}$ , reflection, external quantum efficiency, and photovoltaic efficiency—antireflection coatings were evaluated using the TCAD (technology computer-aided design) Sentaurus. TCAD is restricted to either one or two dimensions.

There have been studies on the thickness variations of a Perovskite layer through the spectral wavelength bands ranging from 100 nm to 1300 nm. There have also been discussions on the influence of the thickness of absorber layers on the performance of Perovskite solar cells with SCAPS software. Moreover, the results of a short-circuit density current device of 20.991 mAcm<sup>-2</sup>, an open circuit voltage device of 0.741 V, a fill factor device percentage ratio of 54.048%, and a power conversion solar cell device efficiency of 8.256% were demonstrated. The solar cell device quantum internal efficiency clarified a strong activity through the visible spectrum region. The authors clarified the defective solar cell design parameters of the interfaces and absorber layers. A solar cell structure simulation and solar cell energy level diagram were also constructed [24]. The authors clarified the power conversion efficiency optimization in multi-band solar cells. They then conducted a theoretical investigation with a genetic optimization algorithm. They showed a three- and four-band diagram of solar cell devices. The authors then used a genetic algorithm optimization technique for the estimation of the peak quantum efficiency of used multi-band solar cell devices. Their results achieved a maximum quantum efficiency for three- and four-band solar cells, which were 62.9% and 70.3%, respectively [25]. The authors designed and characterized effective solar cell devices. They then clarified a two-stage multi-band framework optimization for the full solar cell device structure design. The solar cell design was clarified through solar cell characterization, solar cell cost minimization, and internal quantum device efficiency maximization. The evaluation of fifteen structures for various solar cell design simulations was worked on, and this was achieved through the material type variations and photodiode doping strategies. In addition, the authors concluded that through a solar cell design, as well as a comparison and optimization of the doped zinc oxide layer (which is based on the transparent conductive oxide (TCO) layer

and rough silver back reflector (BR)), internal quantum efficiency can be optimized. This proposed study reported a total internal quantum efficiency of 60.31% [26].

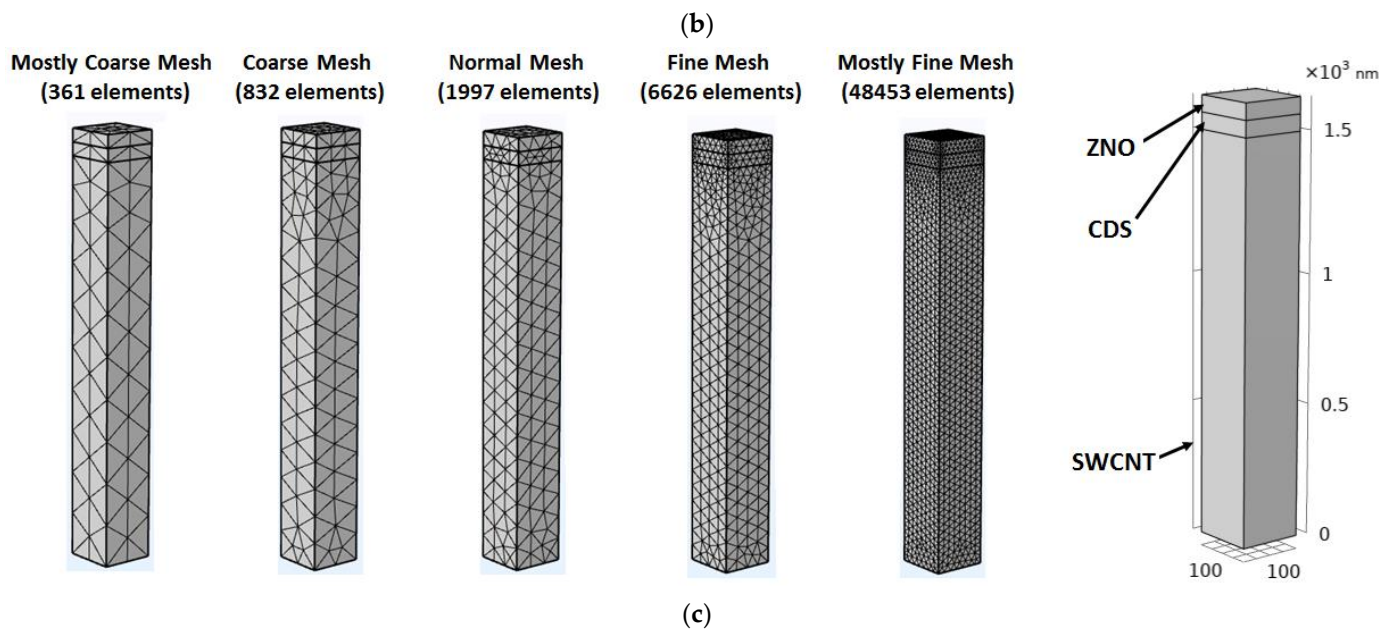
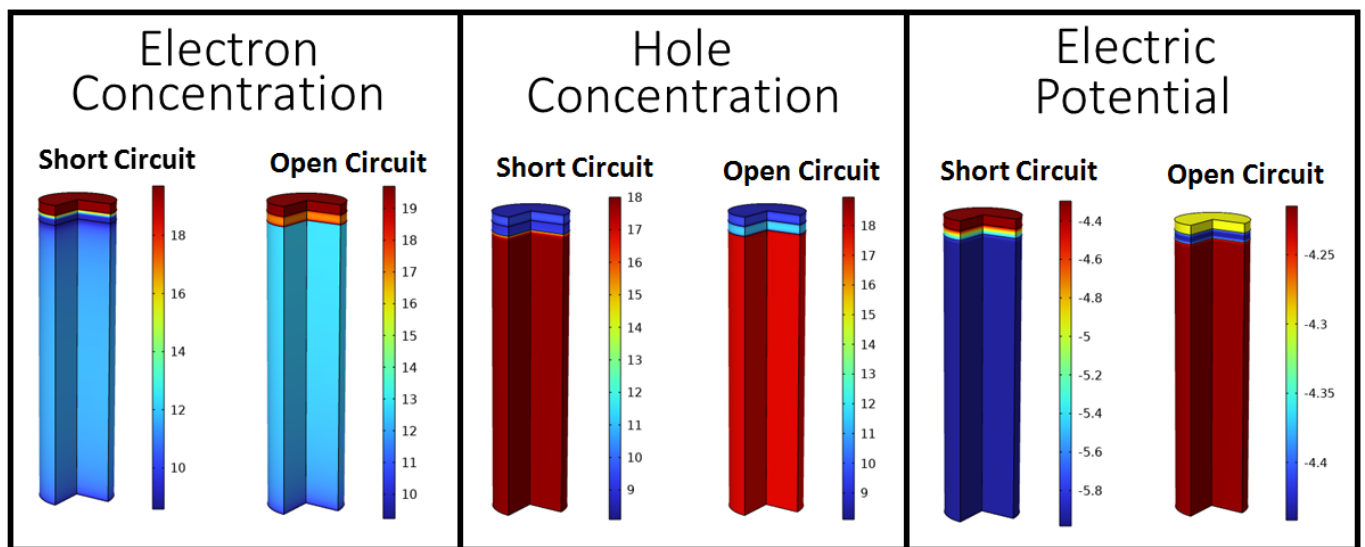
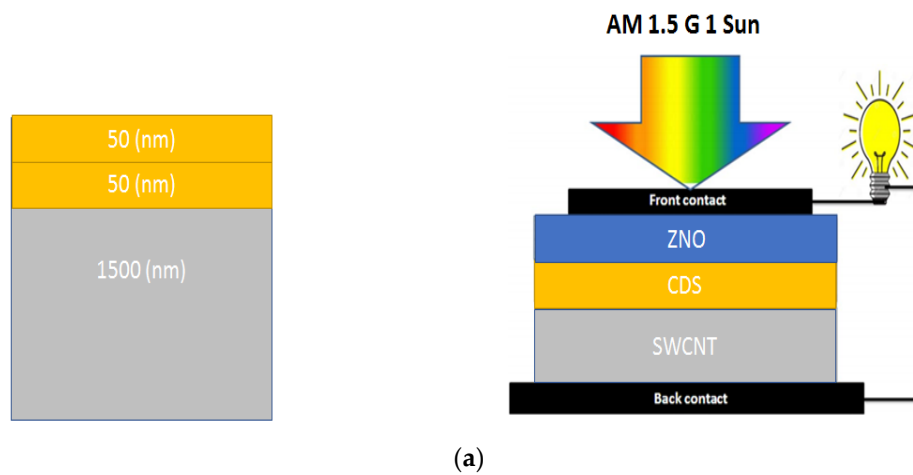
Certain authors have investigated the power conversion efficiency limitation factors of Cu (In<sub>x</sub>Ga<sub>1-x</sub>) (Se)<sub>2</sub> thin-film solar cells using SCAPS simulation software. They have studied the effects of the various layers doping levels and series resistance of solar cell structure design on short-circuit current density, open circuit voltage, total conversion power efficiency, and fill factor percentage. They have concluded that an increase in the solar cell's layer series resistance causes a decrease in the conversion power efficiency with a light intensity dependency. In addition, the absorber doping level and layer buffer played an important vital role in the control of the solar cells' conversion power efficiency; moreover, they help in filling solar cell factor values with peak values when the doping levels of acceptors are approximately equal to the doping levels of donors [27].

Other scholars have provided more details about the study of the conversion of solar energy systems when using the maximum power point method. They have the key to clarifying the detailed procedures of this proposed technique with the tracking process for the solar cell panel with both standalone and grid connections in the solar cells' energy conversion system when using a boost converter. The solar cell equivalent circuit design with I–V solar cell characteristics through different areas has been presented. In addition, the PV array impedance against applied voltage has been presented, as well as the sketched boost converter impedance against a duty cycle. Moreover, these authors have elaborated on power conversion efficiencies versus the voltage curves for the irradiances of 800 W/m<sup>2</sup> and 700 W/m<sup>2</sup>, as well as on their maximum power peak points. They have performed all the simulation solar cell results by using MATLAB/Simulink to demonstrate the better-proposed scheme performance [28].

## 2. Different Suggested Solar Cell Structure Descriptions

The suggested solar cell structure descriptions are shown in Table 1, and the basic front and back contacts are clarified in Figure 1a. The solar cell structure is composed of a single-walled carbon nanotube (SWCNT) layer thickness of 1500 nm, a cadmium sulfide (CdS) layer thickness of 50 nm, and a zinc oxide (ZnO) layer thickness of 50 nm. This was set for the purpose of upgrading the solar cell performance signature. Figure 1b demonstrates a three-dimensional schematic view of the short and open circuits of the electrons, hole concentrations, and electric potential. The COMSOL mesh modeling (triangle elements with a constant shape function) is clarified in Figure 1c.

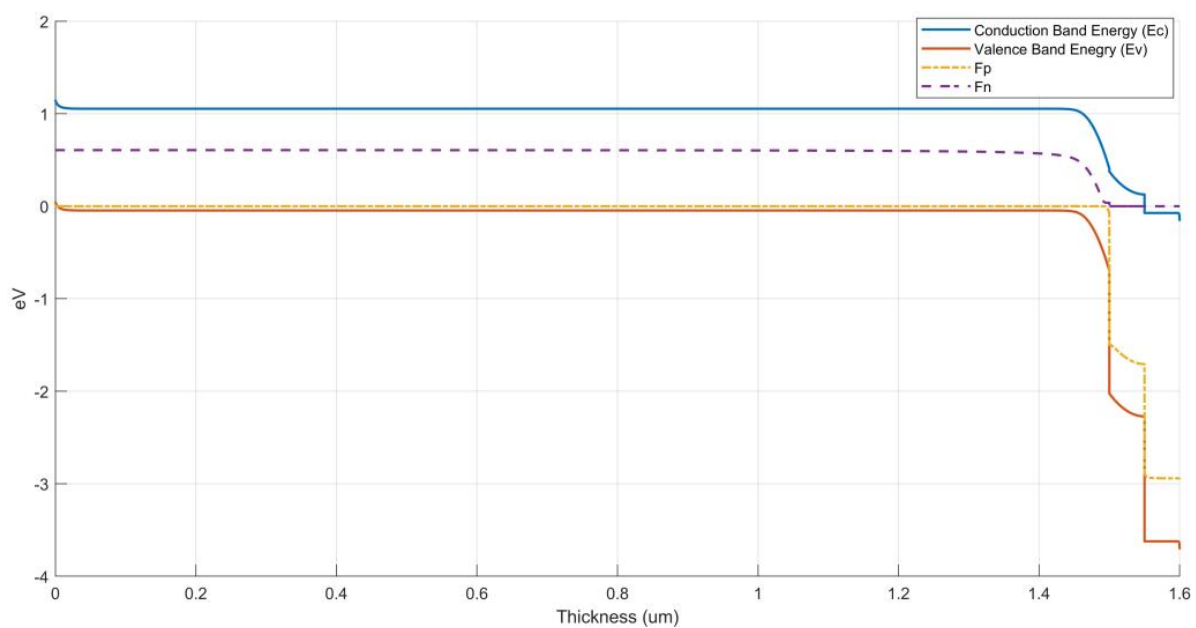
Figure 2 clarifies the conduction and valence band energy diagrams of the layer thickness variations for the suggested solar cell structure. The quantum efficiency versus the spectral wavelength band is clarified in Figure 3 for the suggested solar cell structure. The quantum efficiency ranges approximately from 83.5% to 99.23% through the spectral wavelength band of 250 nm to 360 nm. However, the quantum efficiency is approximately 99.999% through the spectral wavelength band of 360 nm to 1000 nm. The quantum efficiency degrades from 99.99% to the lowest values through the spectral wavelength band of 1000 nm to 1500 nm. Then, we can conclude that the best region of the solar cell performance operation through the spectral wavelength band is from 360 nm to 1000 nm. Figure 4 demonstrates the carrier generation–recombination rate versus the layer thickness of the suggested solar cell structure. Figure 5 shows the light current density versus the bias voltage (J/V characteristics curve) of the proposed solar cell structure. It is evident that the photo-current density is almost constant at 8 mA/cm<sup>2</sup> when applied to the bias voltage (which ranges from 0 V to 1.75 V). Figure 6 illustrates the photon energy versus the spectral wavelength band of the suggested solar cell structure. Figure 7 illustrates the short-circuit current density and maximum power variations versus the applied bias voltage.



**Figure 1.** (a) Suggested solar cell structure in a schematic view. (b) The 3-D short and open circuits of the electrons, hole concentrations, and electric potential. (c) COMSOL mesh modeling (the triangle elements with a constant shape function).

**Table 1.** Basic material layer structures of the suggested solar cell [29–31].

Parameters	AlN	CdS	CBTS	ZnO:Al	SWCNT	ZnS	GaP
Thickness (nm)	----	----	----	----	----	----	----
Band gap (eV)	6.42	2.4	1.9	3.55	1.1	3.5	2.26
Electron affinity (eV)	0.6	4.3	3.6	4.5	4.27	4.5	3.8
Dielectric permittivity	8.9	8.73	5.4	8.96	3.4	10	11.1
CB effective density of the states ( $1/\text{cm}^3$ )	$6.3 \times 10^{18}$	$2.2 \times 10^{18}$	$2.2 \times 10^{18}$	$2.94 \times 10^{18}$	$5 \times 10^{16}$	$1.5 \times 10^{18}$	$1.8 \times 10^{19}$
VB effective density of states ( $1/\text{cm}^3$ )	$4.8 \times 10^{20}$	$1.8 \times 10^{19}$	$1.8 \times 10^{19}$	$2.98 \times 10^{18}$	$6 \times 10^{17}$	$1.8 \times 10^{18}$	$1.9 \times 10^{19}$
Electron thermal velocity (cm/s)	$1.85 \times 10^7$	$10^7$	$10^7$	$1 \times 10^7$	$10^7$	$1 \times 10^7$	$2 \times 10^7$
Hole thermal velocity (cm/s)	$0.41 \times 10^7$	$10^7$	$10^7$	$1 \times 10^7$	$10^7$	$1 \times 10^7$	$1.3 \times 10^7$
Electron mobility ( $\text{cm}^2/\text{Vs}$ )	300	160	30	46	$8 \times 10^4$	50	250
Hole mobility ( $\text{cm}^2/\text{Vs}$ )	14	15	10	26	$2 \times 10^3$	20	150
Donor density ( $1/\text{cm}^3$ )	----	$10^{17}$	----	$5 \times 10^{19}$	----	$2 \times 10^{17}$	----
Acceptor density ( $1/\text{cm}^3$ )	$10^{18}$	-----	$10^{17}$	----	$10^{17}$	-----	$10^{18}$
Defect density ( $1/\text{cm}^3$ )	$1 \times 10^{17}$	$1 \times 10^{17}$	$1 \times 10^{15}$	$3.4 \times 10^{20}$	$1 \times 10^{14}$	$3.02 \times 10^{19}$	$2 \times 10^{15}$

**Figure 2.** Conduction and valence band energy diagram of the layer thickness variations for the suggested solar cell structure.

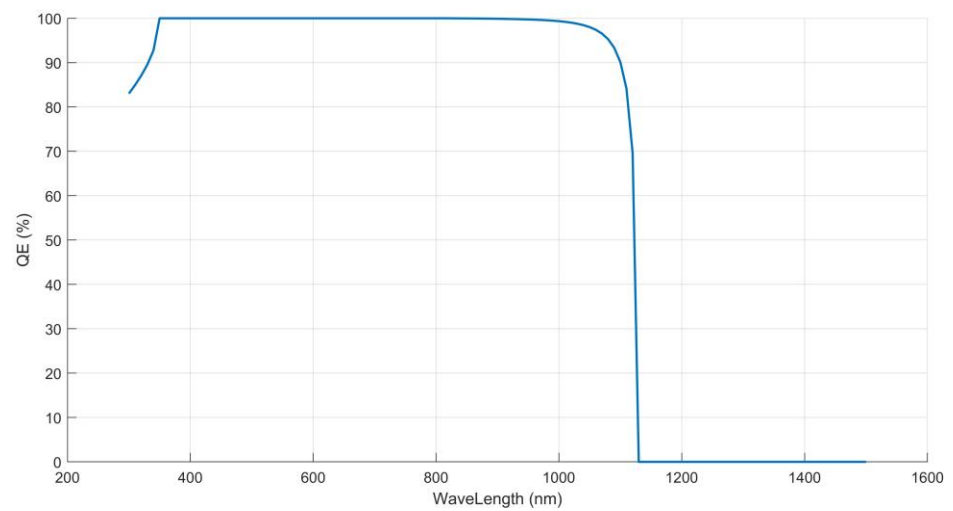


**Figure 3.** Quantum efficiency versus the spectral wavelength band for the suggested solar cell structure.

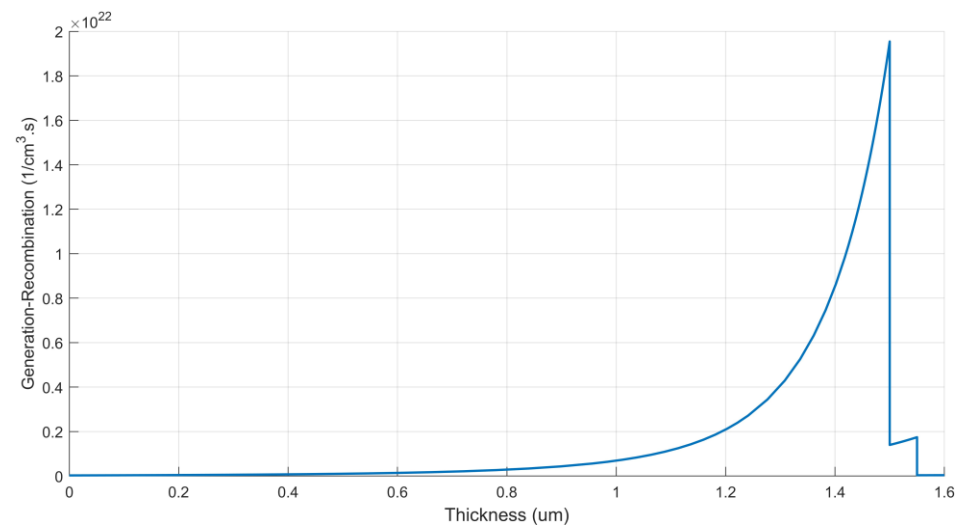


**Figure 4.** Carrier generation–recombination rate versus the layer thickness of the suggested solar cell structure.

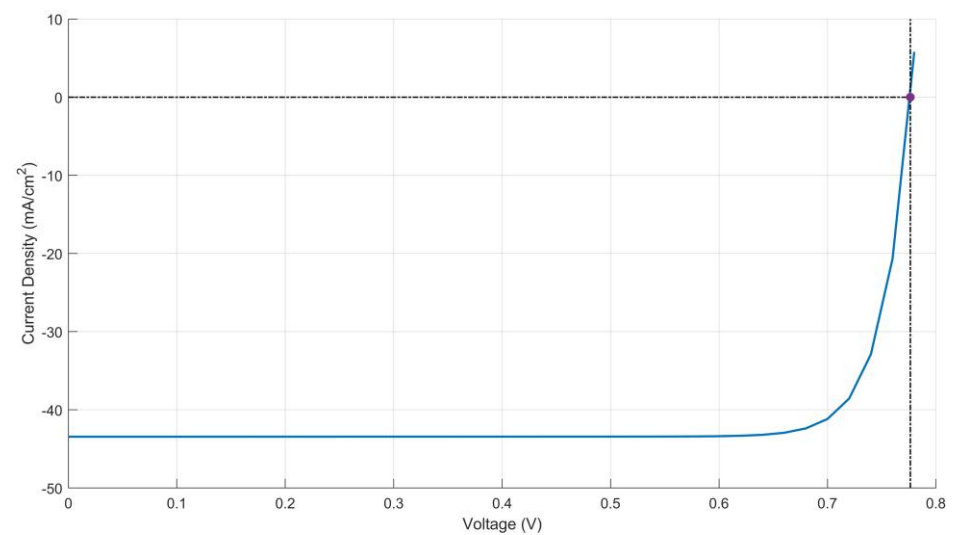


**Figure 5.** Light current density versus the bias voltage of the suggested solar cell structure.

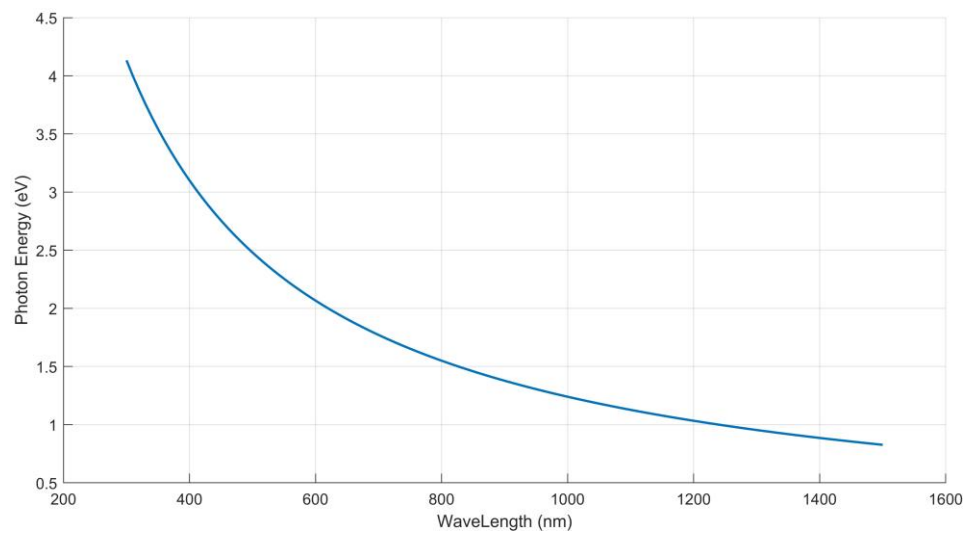


Figure 6. Photon energy versus the spectral wavelength band of the suggested solar cell structure.

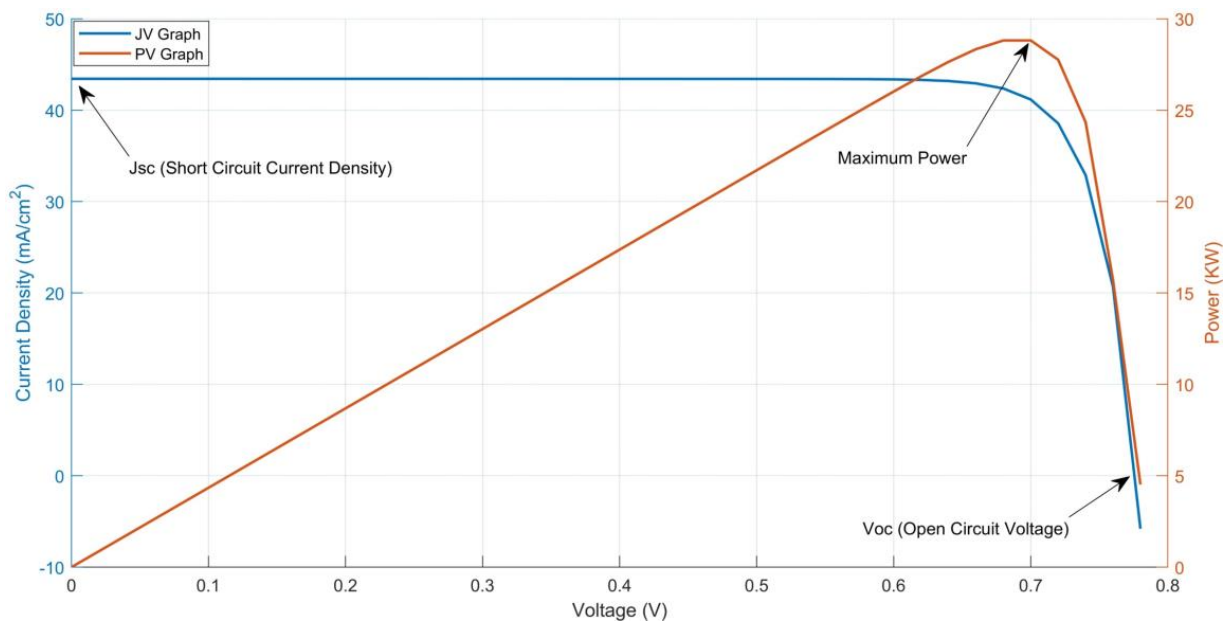


Figure 7. Short-circuit current density and maximum power variations versus the applied bias voltage.

### 3. Solar Cell Design and Modeling Equations

The SCAPS-1D model is controlled by the solution of the basic semiconductor equations of the hole and electron continuities, and this is in addition to the Poisson equations.

$$\text{div}(\epsilon \nabla \Psi) = -\rho \tag{1}$$

The continuity equations of the electron and hole carriers:

$$\frac{\partial n}{\partial t} = \frac{1}{q} \text{div}(\vec{j}_n) + G_n - R_n \tag{2}$$

$$\frac{\partial p}{\partial t} = \frac{1}{q} \text{div}(\vec{j}_p) + G_p - R_p \tag{3}$$

where

$p, n$ : The hole and electron concentrations.

$J_p, J_n$  : The hole and electron densities.

$G_n, G_p$ : The electron and hole generation rates.

$R_n, R_p$ : The electron and hole recombination rates.

The proposed solar cell layer structures are illustrated in Table 1. The surface planar morphology is studied with an AM 1.5 G1 illumination spectrum. The light path length in the light trapping model is as follows [32]:

$$Z = 4 + \ln\left(n^2 + (1 - n^2) e^{-\alpha W}\right) / \alpha W \quad (4)$$

where  $\alpha$  is the attenuation and  $n$  is the absorptive solar cell refractive index. Moreover, the substrate width ( $W$ ) = 180  $\mu\text{m}$ . The junction current–voltage (JV) density is clarified by the following [33]:

$$J_n = D_n \frac{dn}{dx} + \mu_n n \frac{d\phi}{dx} \quad (5)$$

$$J_p = D_p \frac{dp}{dx} + \mu_p p \frac{d\phi}{dx} \quad (6)$$

where  $n$  and  $p$  are the electronic and hole concentrations, and  $\mu_p$  and  $\mu_n$  represent the hole and electron mobilities.

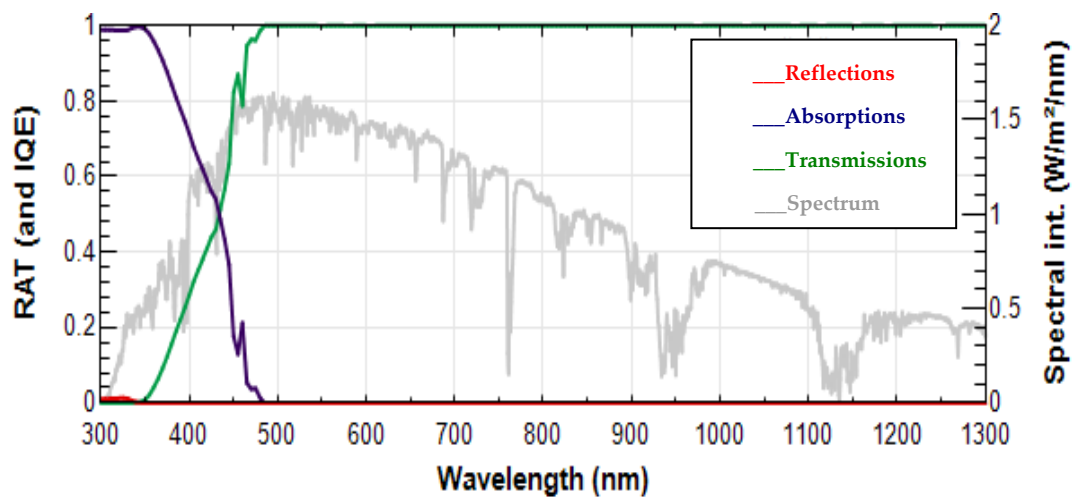
## 4. Results and Discussion

### 4.1. Optimized Solar Cell Structure Design

This section focuses on the optimized solar cell structure design. The integration of the simulation techniques, judicious material selection, and meticulous performance metrics showcase a methodical approach toward creating a solar cell that is capable of achieving high efficiency across a wide spectrum of light in an AM 1.5 G1 sun solar cell illumination spectrum. Having said this, many researchers are still working on the efficiency potential, based on external radiative efficiency (ERE), of high-efficiency solar cells' open-circuit voltage loss and fill factor loss. Conduction and valence band energy diagrams of solar cell design structures are simulated against the layer thickness variations for the suggested solar cell structures. Short-circuit current densities and maximum power variations are clarified versus the bias voltage. Light current density is simulated versus the bias voltage (J/V characteristics curve) of the suggested solar cell design structures. The substrate layer structure is glass material, while the subsequent layer is the transparent conductive oxide layer. The solar cell structure is composed of a single-walled carbon nanotube (SWCNT) layer thickness of 1500 nm, a cadmium sulfide (CdS) layer thickness of 50 nm, and a zinc oxide (ZnO) layer thickness of 50 nm for the purposes of upgrading the solar cell performance signature with the silicon substrate material. In Section 4.2, the clarification of the reflections, absorptions, and transmissions of the proposed photovoltaic solar cell against the spectral wavelength variations are included.

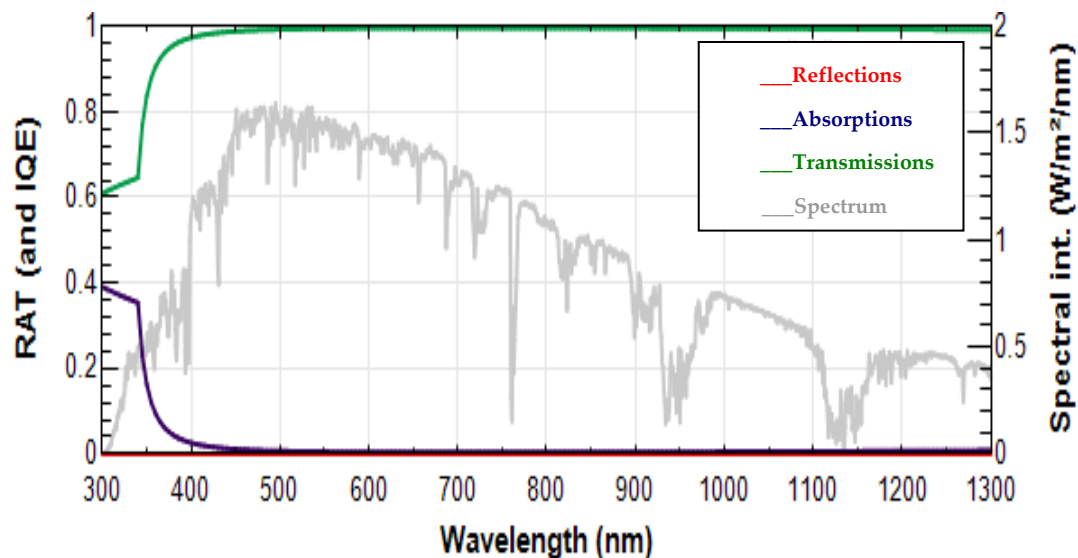
### 4.2. RAT Variations with Spectrum Wavelength Variations

Figure 8 shows the reflections, absorptions, transmissions, and spectral intensities against the spectral wavelengths through the use of the optimum GaP absorber layer thicknesses, and this is achieved by using OPAL 2 solar cell simulation. The total incident photo-current density through a GaP absorber layer was 5.64 mA/cm<sup>2</sup>. Furthermore, the photo-absorbed current in a GaP film was 2.48 mA/cm<sup>2</sup>, and the photo-absorbed current in the substrate was 3.17 mA/cm<sup>2</sup>.



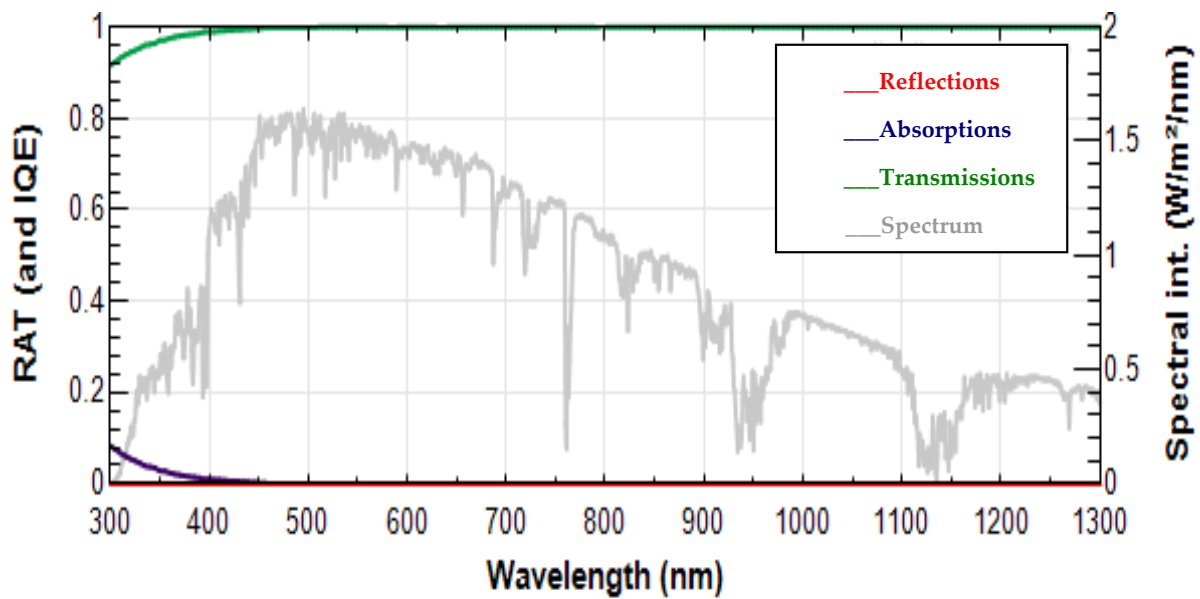
**Figure 8.** The reflections, absorptions, transmissions, and spectral intensities against the spectral wavelengths through the use of optimum GaP absorber layer thickness, which were determined by using OPAL 2 simulation.

Figure 9 illustrates the reflections, absorptions, transmissions, and spectral intensities against the spectral wavelengths, and this was determined through the use of an optimum ZnS absorber layer thickness via OPAL 2 solar cell simulation. The total incident photo-current density through a ZnS absorber layer was  $51.88 \text{ mA/cm}^2$ , the photo-absorbed current in a ZnS film was  $0.48 \text{ mA/cm}^2$ , and the photo-absorbed current in the substrate was  $51.41 \text{ mA/cm}^2$ .



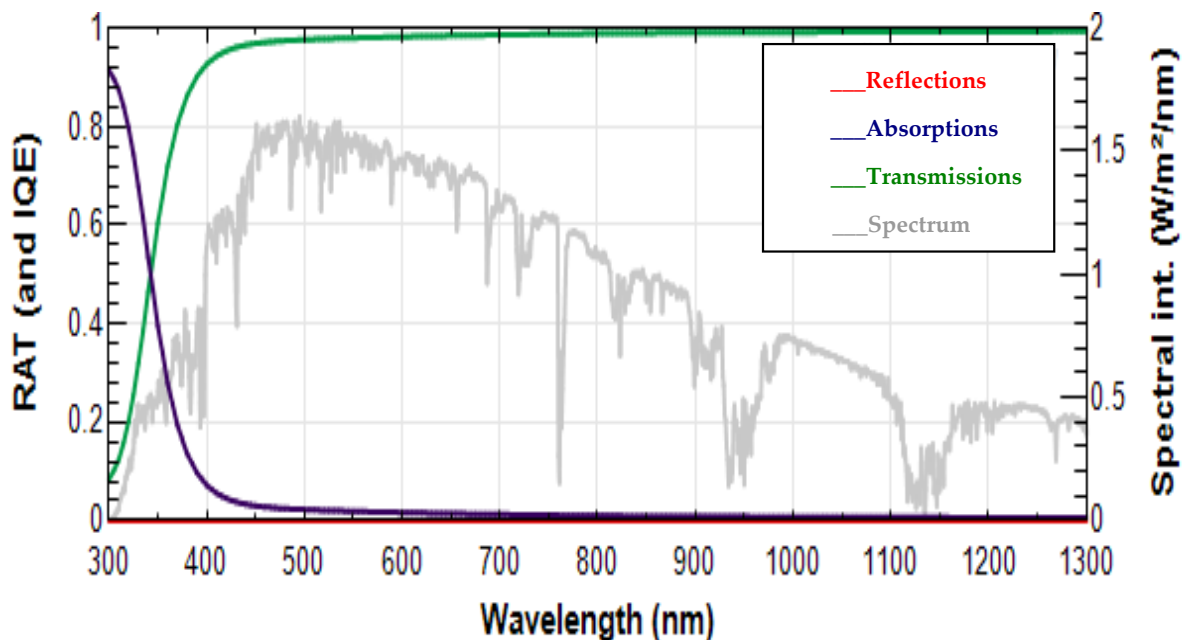
**Figure 9.** The reflections, absorptions, transmissions, and spectral intensities against the spectral wavelengths, which was achieved through the use of optimum ZnS absorber layer thicknesses via OPAL 2 simulation.

Figure 10 demonstrates the reflections, absorptions, transmissions, and spectral intensities against the spectral wavelengths, which was achieved through the use of an optimum AlN absorber layer thickness via OPAL 2 solar cell simulation. The total incident photo-current density through an AlN absorber layer was  $6.97 \text{ mA/cm}^2$ , the photo-absorbed current in an AlN film was  $0.05 \text{ mA/cm}^2$ , and the photo-absorbed current in the substrate was  $6.93 \text{ mA/cm}^2$ .



**Figure 10.** The reflections, absorptions, transmissions, and spectral intensities against the spectral wavelengths, which was achieved through the use of an optimum AlN absorber layer thickness via OPAL 2 simulation.

Figure 11 indicates the reflections, absorptions, transmissions, and spectral intensities against the spectral wavelengths through the use of an optimum ZnO:Al absorber layer thickness via OPAL 2 solar cell simulation. The total incident photo-current density through a ZnO:Al absorber layer was  $51.88 \text{ mA/cm}^2$ , the photo-absorbed current in a ZnO:Al film was  $1.06 \text{ mA/cm}^2$ , and the photo-absorbed current in the substrate was  $50.82 \text{ mA/cm}^2$ .



**Figure 11.** The reflections, absorptions, transmissions, and spectral intensities against the spectral wavelengths through the use of an optimum ZnO:Al absorber layer thickness via OPAL 2 simulation.

Figure 12 shows the reflections, absorptions, transmissions, and spectral intensities against spectral wavelengths through the use of an optimum CdS absorber layer thickness via OPAL 2 solar cell simulation. The total incident photo-current density through a CdS absorber layer was  $51.88 \text{ mA/cm}^2$ , the photo-absorbed current in a CdS film was

9.87 mA/cm<sup>2</sup>, and the photo-absorbed current in the substrate was 42.01 mA/cm<sup>2</sup>. In Section 4.3, the surface morphology variation effects on the absorbed photo-current and internal quantum efficiencies are demonstrated.

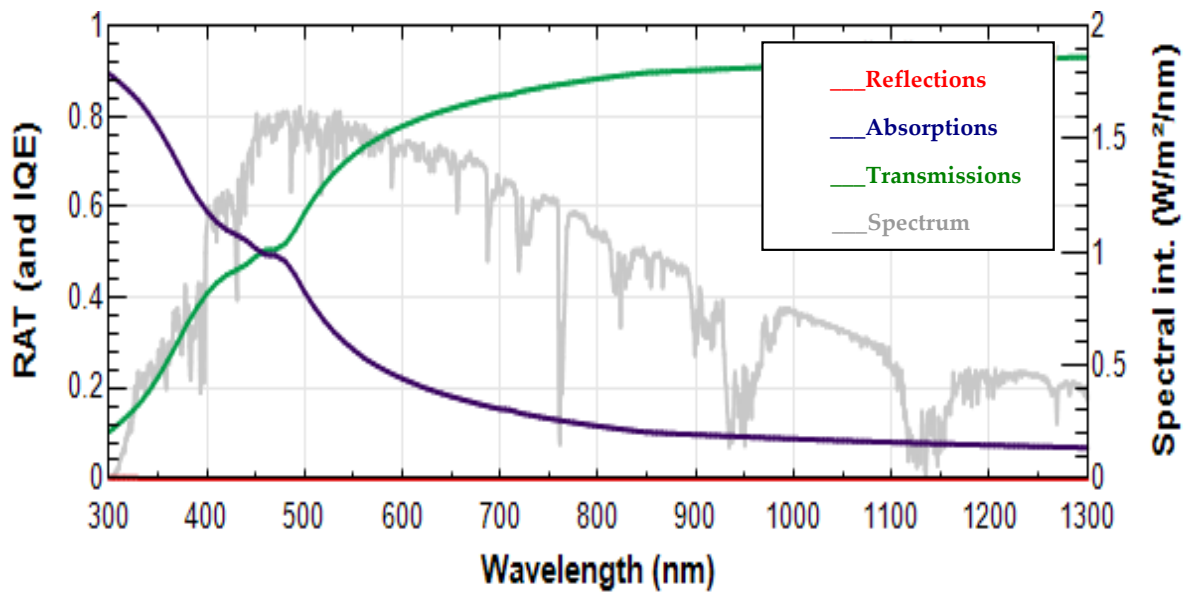


**Figure 12.** The reflections, absorptions, transmissions, and spectral intensities against the spectral wavelengths through the use of an optimum CdS absorber layer thickness via OPAL 2 simulation.

4.3. Effects of the Surface Morphology on the Photo-Current Absorption and IQE

Figure 13 illustrates the substrate absorption current and the quantum efficiency versus the different substrate surface configurations. The substrate absorption current and quantum efficiency were 64 mA/cm<sup>2</sup> and 93%, respectively, in the case of planar substrate surface configuration. For the V grooves' surface configuration, the substrate absorption current and quantum efficiency were 66 mA/cm<sup>2</sup> and 94%, respectively.

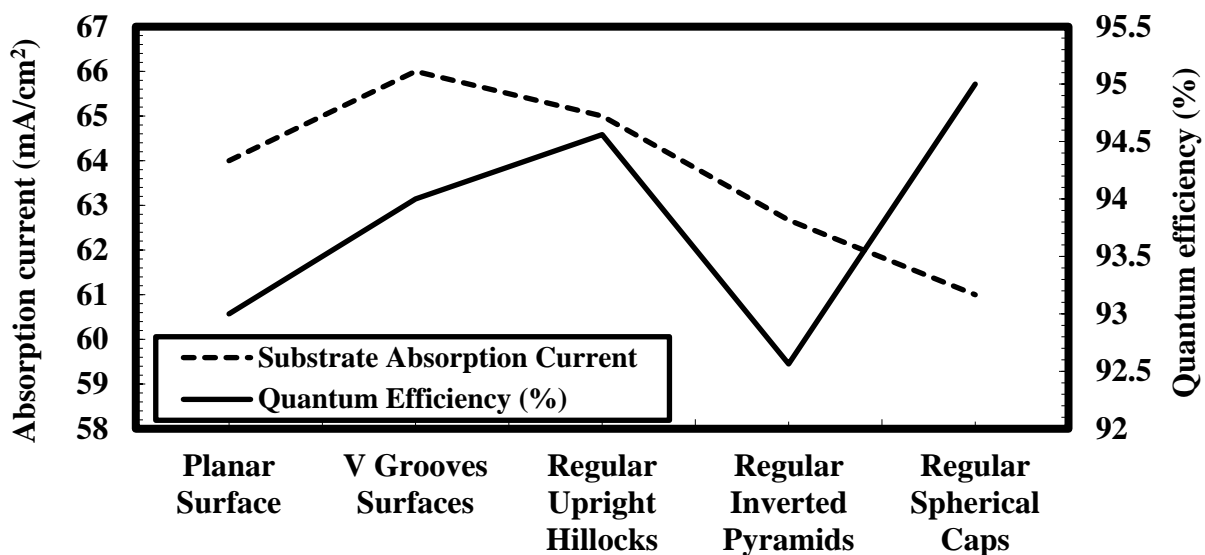


**Figure 13.** The substrate absorption current and quantum efficiency versus the different substrate surface configurations.

The substrate absorption current and quantum efficiency were 65 mA/cm<sup>2</sup> and 94.65%, respectively, in the case of the regular upright hillocks' substrate surface configurations. The substrate absorption current and quantum efficiency were 62.67 mA/cm<sup>2</sup> and 92.675%,

respectively, in the case of the regular inverted pyramids' substrate surface configurations. The substrate absorption current and quantum efficiency were  $61 \text{ mA/cm}^2$  and  $95\%$ , respectively, in the case of the regular spherical caps' surface configurations. The planar surface V grooves' surface and regular spherical caps were the best candidates for the substrate's surface configuration for the enhancement of the quantum efficiency of the solar cells. In Section 4.4, the suggested substrate materials' variation effects on the photo-current absorption and internal quantum efficiency are shown.

#### 4.4. Substrate Materials' Variation Effects on the Photo-Current Absorption and IQE

Figure 14 demonstrates the substrate absorption current and quantum efficiency versus the different substrate layer structures. The substrate absorption current and quantum efficiency were  $49 \text{ mA/cm}^2$  and  $73\%$ , respectively, in the case of the  $\text{MgF}_2$  substrate layer. The substrate absorption current and quantum efficiency were  $55 \text{ mA/cm}^2$  and  $82\%$ , respectively, in the case of the  $\text{SiN}_x$  substrate layer. The substrate absorption current and quantum efficiency were  $62 \text{ mA/cm}^2$  and  $93\%$ , respectively, in the case of the  $\text{SiO}_x$  substrate layer.

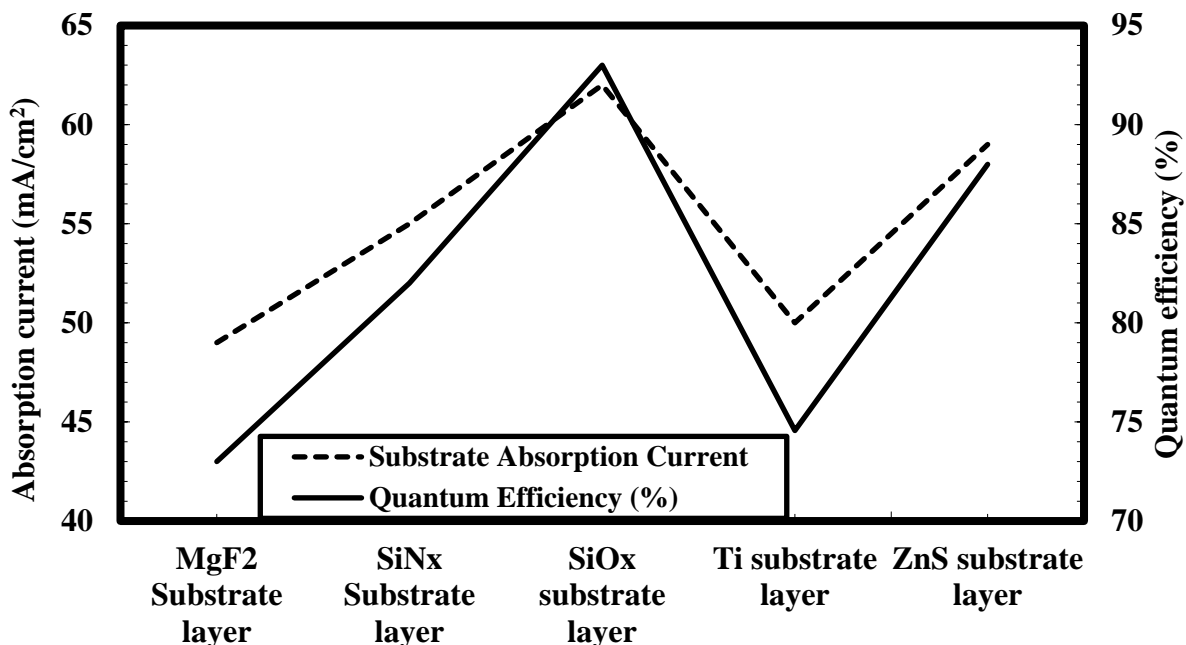


Figure 14. The substrate absorption current and quantum efficiency versus the different substrate layer structures.

The substrate absorption current and quantum efficiency were  $50 \text{ mA/cm}^2$  and  $74.654\%$ , respectively, in the case of the Ti substrate layer. The substrate absorption current and quantum efficiency were  $59 \text{ mA/cm}^2$  and  $88\%$ , respectively, in the case of the ZnS substrate layer. The ZnS substrate layer was found to be the best candidate material substrate structure for upgrading the proposed solar cell's internal quantum efficiency. In Section 4.5, the absorber material layer variation effects on the photo-current absorption and internal quantum efficiency are clarified.

#### 4.5. Absorber Material Layer Variation Effects on the Photo-Current Absorption and IQE

Figure 15 clarifies the substrate absorption current and quantum efficiency versus the different absorber layer structures. The substrate absorption current and quantum efficiency were  $62.5 \text{ mA/cm}^2$  and  $93\%$ , respectively, in the case of the  $\text{TiO}_2$  absorber layer. The substrate absorption current and quantum efficiency were  $61 \text{ mA/cm}^2$  and  $91\%$ , respectively, in the case of the ITO absorber layer. The substrate absorption current and quantum efficiency were  $52 \text{ mA/cm}^2$  and  $78\%$ , respectively, in the case of the CdTe

absorber layer. The substrate absorption current and quantum efficiency were  $52 \text{ mA/cm}^2$  and  $78\%$ , respectively, in the case of the CdTe absorber layer. The substrate absorption current and quantum efficiency were  $53 \text{ mA/cm}^2$  and  $80\%$ , respectively, in the case of the CdS absorber layer.

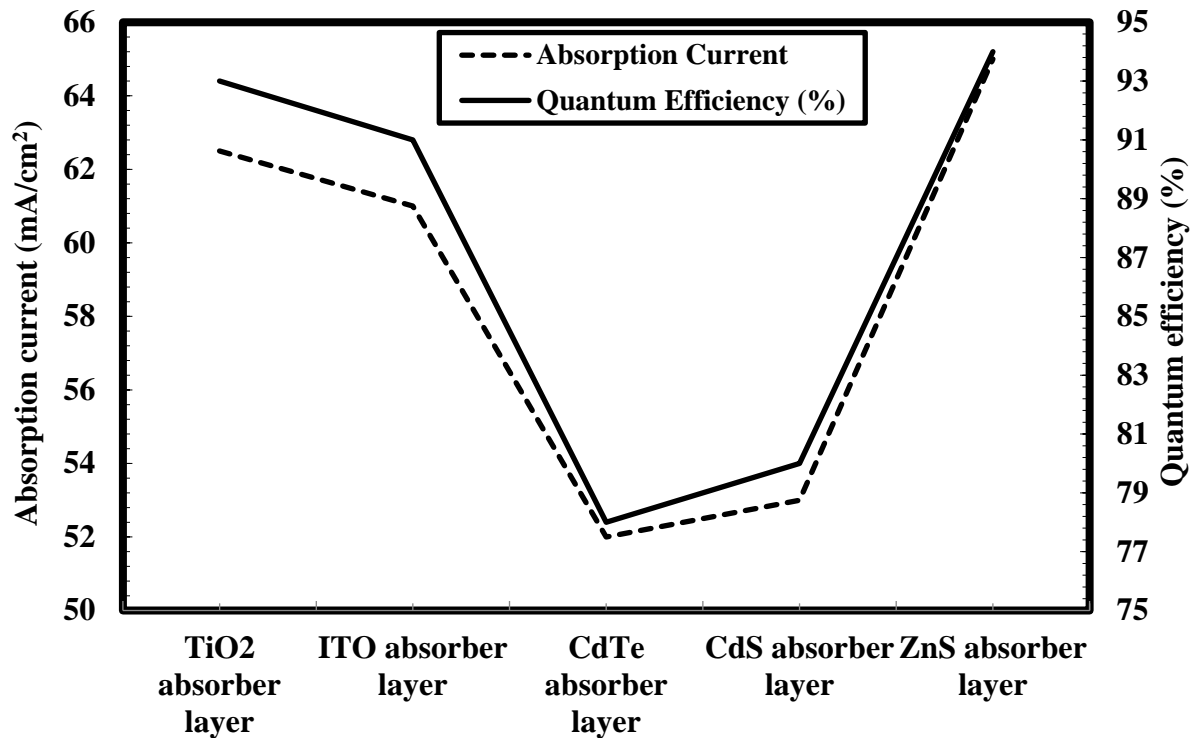


**Figure 15.** Substrate absorption current and quantum efficiency versus different absorber layer structures.

The substrate absorption current and quantum efficiency were  $65 \text{ mA/cm}^2$  and  $94\%$ , respectively, in the case of the ZnS absorber layer. The TiO<sub>2</sub> absorber layer and ZnS absorber layer were the best candidate material structures for the absorber layer of the solar cells. In Section 4.6, the contact layer material variation effects on the photo-current absorption and internal quantum efficiency are clarified.

#### 4.6. Contact Layer Material Variation Effects on the Photo-Current Reflection/Absorption and IQE

Figure 16 shows the substrate absorption current and quantum efficiency versus the different contact layer structures. The substrate absorption current and quantum efficiency were  $60 \text{ mA/cm}^2$  and  $89\%$ , respectively, in the case of the TiO<sub>2</sub> contact layer. The substrate absorption current and quantum efficiency were  $55 \text{ mA/cm}^2$  and  $84\%$ , respectively, in the case of the Si<sub>3</sub>N<sub>4</sub> contact layer. The substrate absorption current and quantum efficiency were  $50 \text{ mA/cm}^2$  and  $75\%$ , respectively, in the case of the InP contact layer.

The substrate absorption current and quantum efficiency were  $52 \text{ mA/cm}^2$  and  $78\%$ , respectively, in the case of the GaAs contact layer. The substrate absorption current and quantum efficiency were  $62 \text{ mA/cm}^2$  and  $94.6567\%$ , respectively, in the case of the GaP contact layer. The GaP contact layer was the best candidate material structure for the contact layer of the solar cells. In Section 5, the equivalent circuit model and circuit performance parameters optimization are clarified.

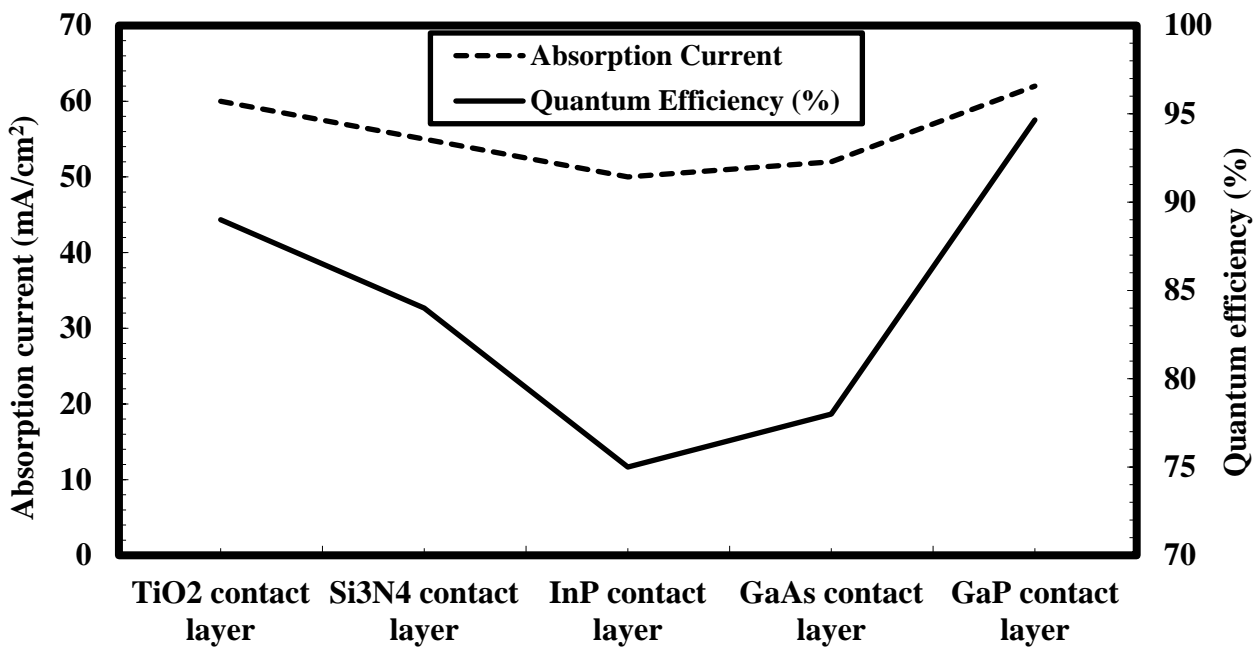


Figure 16. Substrate absorption current and quantum efficiency versus the different contact layer structures.

### 5. Equivalent Circuit Modeling and Circuit Performance Parameter Optimization

The equivalent circuit model diagram of the solar cell device is illustrated in Figure 17. The light-collected current ( $J_L$ ) was  $66.45 \text{ mA/cm}^2$ , and the input solar cell circuit parameters were as follows: the light-collected current ( $J_L$ ) was  $51.88 \text{ mA/cm}^2$ , the saturation current was ( $J_1$ ) =  $1 \text{ pA/cm}^2$ , the saturation current was ( $J_2$ ) =  $1 \text{ nA/cm}^2$ , the saturation current was ( $J_H$ ) =  $100 \text{ pA/cm}^2$ , the resistance ( $R_H$ ) =  $1000 \text{ } \Omega \cdot \text{cm}^2$ , the shunt resistance ( $R_{SH}$ ) =  $100 \text{ k}\Omega \cdot \text{cm}^2$ , and the series resistance ( $R_S$ ) =  $1200 \text{ } \Omega \cdot \text{cm}^2$ . The light JV outputs were as follows: max-power voltage  $V_{mp} = 503.559 \text{ mV}$ , max-power current  $J_{mp} = 48.8075 \text{ mA/cm}^2$ , open-circuit voltage  $V_{oc} = 637.552 \text{ mV}$ , short-circuit current  $J_{sc} = 51.8738 \text{ mA/cm}^2$ , fill factor ( $FF$ ) =  $0.7431$ , and the power conversion efficiency was approximately ( $\eta$ ) =  $29.91\%$ .

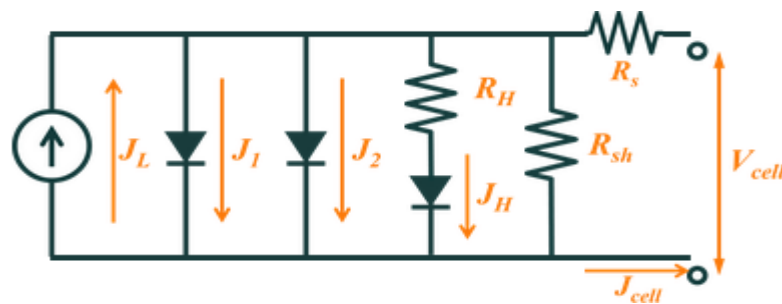


Figure 17. Solar cell circuit model design.

The maximum open-circuit voltage solar cells can be optimized and obtained through the following equation [33]:

$$V_{oc} = \frac{nkT}{q} \ln \left( \frac{I_L}{I_0} \right) + 1 \tag{7}$$

where  $I_0$  and  $I_L$  and are the dark and photo saturation currents, respectively;  $T$  is the temperature; and  $q$  is the charge of the electrons. The maximum power point solar cell was clarified as a function of the  $FF$  parameter. The short-circuit current and the open-circuit voltage were as follows [33]:

$$P_{mp} = FF V_{oc} I_{sc} \tag{8}$$

The power conversion efficiency of the solar cell device was estimated by the following [15]:

$$\eta = \frac{I_{sc} V_{oc} FF}{P_{in}} \quad (9)$$

Figure 18 shows the solar cell photo-current density versus the bias voltage variations. The solar cell photo-current density was 0.12 mA/cm<sup>2</sup> in the short circuit case at a bias voltage of 0.1 Volt, and its value was 0.18 mA/cm<sup>2</sup> in the open-circuit case at a bias voltage of 0.1 Volt. The solar cell photo-current density was 0.42 mA/cm<sup>2</sup> in the short-circuit case at a bias voltage of 0.5 Volt, and its value was 0.55 mA/cm<sup>2</sup> in the open-circuit case at a bias voltage of 0.5 Volt. The solar cell photo-current density was 0.835 mA/cm<sup>2</sup> in the short-circuit case at a bias voltage of 0.9 Volt, and its value was 1.023 mA/cm<sup>2</sup> in the open-circuit case at a bias voltage of 0.9 Volt. The solar cell photo-current density was 1.563 mA/cm<sup>2</sup> in the short-circuit case at a bias voltage of 1.1 Volt, and its value was 1.892 mA/cm<sup>2</sup> in the open-circuit case at a bias voltage of 1.1 Volt.

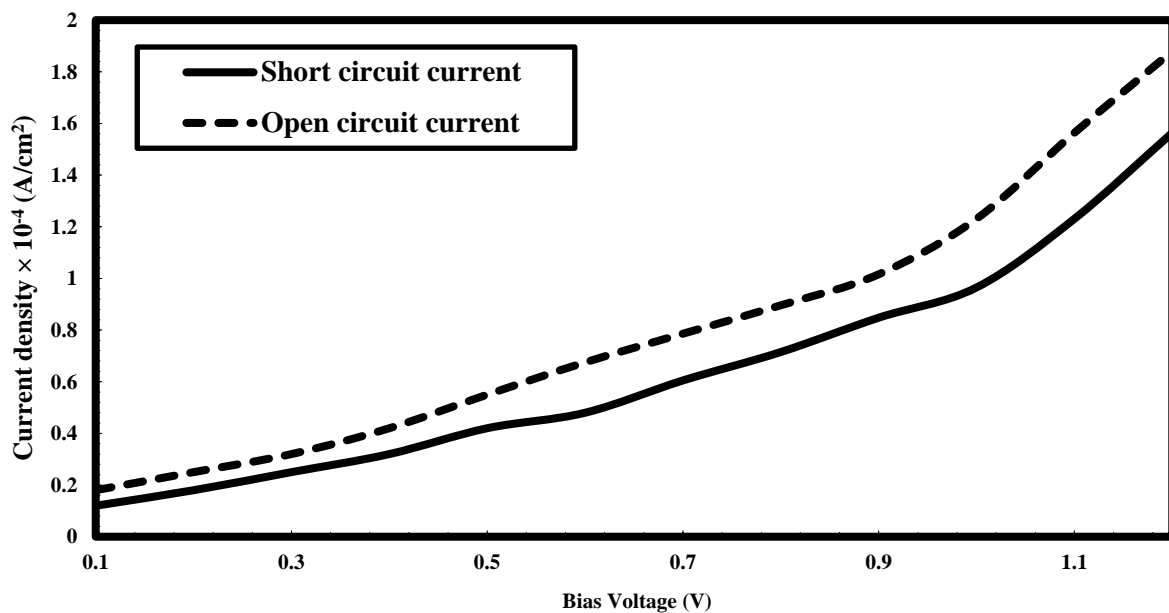


Figure 18. Solar cell photo-current density versus the bias voltage variations.

The basic definition of the ideality factor derivations from the dark IV characteristics curve or the light IV curve was determined. The examination of the recombination in the device was a powerful tool for the ideality factor. When the saturation current was stable, this resulted in the ideality factor also being stable. When the operation is at a low voltage, the shunt resistance tests the performance of the solar cell device and can cause a large peak. It is particularly important to work on the suitable values of shunt resistance to avoid any bad effects on the ideality factor. The temperature and noise have based effects on the ideality factor of the solar cell output measurement. The series resistance variations can cause a large peak at high bias voltages. Figure 19 illustrates the solar cell ideality factor versus the bias voltage variations. The ideality factor was 3.77 in the case of the open-circuit current, and the ideality factor was 3.987 in the case of light current at an applied bias voltage of 0.1 Volt. The ideality factor was 5.56 in the case of the open-circuit current, and the ideality factor was 7.56 in the case of the light current at an applied bias voltage of 0.5 Volt. The ideality factor was 8.32 in the case of the open-circuit current, and the ideality factor was 9.45 in the case of light current at an applied bias voltage of 0.9 Volt. The ideality factor was 3.775 in the case of the open-circuit current, and the ideality factor was 3.9778 in the case of light current at an applied bias voltage of 1.1 Volt. Figure 20 shows the open-circuit voltage and short-circuit current density of the solar cell structure against the GaP absorber layer thickness. It was observed that, in the case of the GaP absorber layer thickness, there

was an increase in both the open-circuit voltage and short-circuit current values. At a 55 nm GaP absorber layer thickness, the  $V_{oc} = 1.701$  mV and the  $J_{sc} = 1.845$  mA/cm<sup>2</sup>. At a 70 nm GaP absorber layer thickness, the open-circuit voltage  $V_{oc}$  was 1.706 mV and the short-circuit current  $J_{sc}$  was 2.242 mA/cm<sup>2</sup>. At a 100 nm GaP absorber layer thickness, the  $V_{oc} = 1.713$  mV and the  $J_{sc} = 2.939$  mA/cm<sup>2</sup>. At a 120 nm GaP absorber layer thickness, the open-circuit voltage  $V_{oc}$  was 1.72 mV and the short-circuit current  $J_{sc}$  was 3.362 mA/cm<sup>2</sup>. At a 250 nm GaP absorber layer thickness, the  $V_{oc} = 1.732$  mV and the  $J_{sc} = 5.16$  mA/cm<sup>2</sup>. At a 500 nm GaP absorber layer thickness, the open-circuit voltage  $V_{oc}$  was 1.744 mV and the short circuit current  $J_{sc}$  was 6.67 mA/cm<sup>2</sup>. At a 1000 nm GaP absorber layer thickness, the  $V_{oc} = 1.76$  mV and the  $J_{sc} = 7.69$  mA/cm<sup>2</sup>. At a 1500 nm GaP absorber layer thickness, the open-circuit voltage  $V_{oc}$  was 1.775 mV and the short-circuit current  $J_{sc}$  was 8.13 mA/cm<sup>2</sup>. The optimum GaP absorber layer thickness was 1500 nm for the most optimum solar cell conversion efficiency performance.

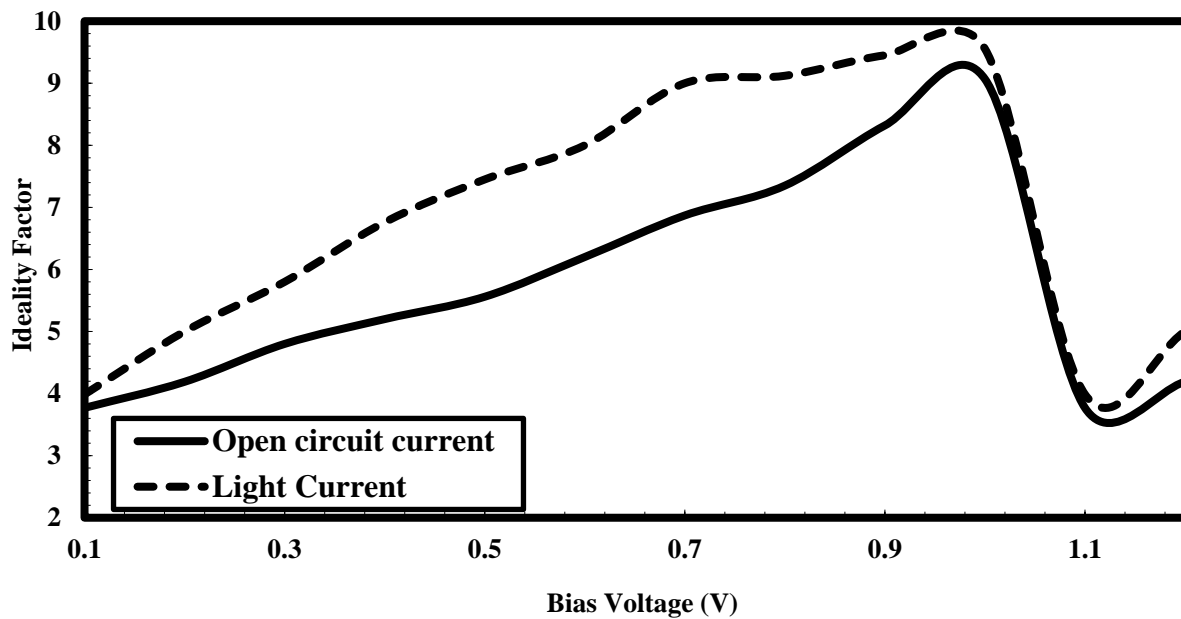


Figure 19. Solar cell ideality factor versus the bias voltage variations.

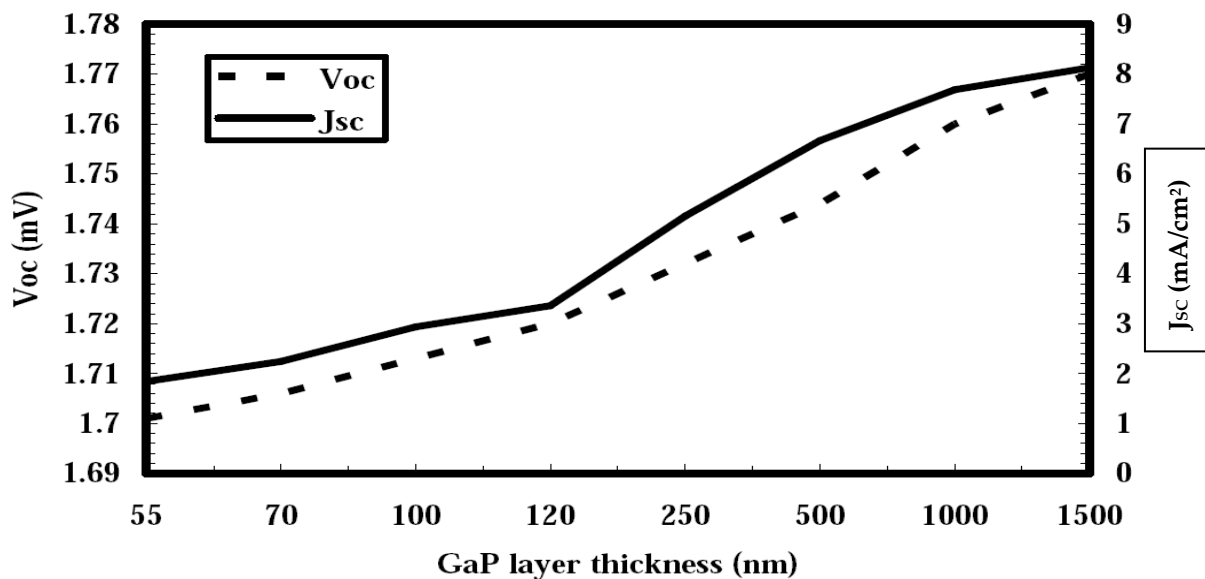


Figure 20. Short-circuit current density/open-circuit voltage of the solar cell structure against the GaP absorber layer thickness.

Figure 21 illustrates the fill factor, power conversion efficiency, and quantum efficiency of the solar cell structure against the GaP absorber layer thickness. With a GaP absorber layer thickness of 55 nm, it was considered that the fill factor, power conversion efficiency, and quantum efficiency were 75.24%, 2.36%, and 40%, respectively. With a GaP absorber layer thickness of 70 nm, it was indicated that the fill factor, power conversion efficiency, and quantum efficiency were 75.09%, 2.87%, and 45%, respectively. The fill factor, power conversion efficiency, and quantum efficiency were 74.97%, 3.77%, and 50% when using a GaP absorber layer thickness of 100 nm. The fill factor, power conversion efficiency, and quantum efficiency were 74.75%, 4.32%, and 60%, respectively, with a GaP absorber layer thickness of 120 nm. The fill factor, power conversion efficiency, and quantum efficiency were 74.91%, 6.69%, and 80%, respectively, with a GaP absorber layer thickness of 250 nm. The fill factor, power conversion efficiency, and quantum efficiency were 75.76%, 8.82%, and 90%, respectively, with a GaP absorber layer thickness of 500 nm. With a GaP absorber layer thickness of 1000 nm, it was indicated that the fill factor, power conversion efficiency, and quantum efficiency were 77.11%, 10.42%, and 92.5%, respectively. The fill factor, power conversion efficiency, and quantum efficiency were 78.02%, 11.2%, and 92.5%, respectively, with a GaP absorber layer thickness of 1500 nm. Figure 22 demonstrates the short-circuit current density/open-circuit voltage of the suggested solar cell structure against a ZnS absorber layer thickness of X nm. At 25 nm, the ZnS absorber layer thickness had a  $V_{oc} = 1.712$  mV and a  $J_{sc} = 2.93$  mA/cm<sup>2</sup>. At 50 nm, the ZnS absorber layer thickness had an open-circuit voltage  $V_{oc}$  of 1.732 mV and short-circuit current  $J_{sc}$  of 5.16 mA/cm<sup>2</sup>. At 55 nm, the ZnS absorber layer thickness had a  $V_{oc} = 1.701$  mV and a  $J_{sc} = 1.845$  mA/cm<sup>2</sup>. In addition, a  $V_{oc} = 1.715$  mV and a  $J_{sc} = 2.947$  mA/cm<sup>2</sup> were estimated at a 75 nm ZnS absorber layer thickness. A  $V_{oc} = 1.716$  mV and a  $J_{sc} = 2.959$  mA/cm<sup>2</sup> were demonstrated at a 100 nm ZnS absorber layer thickness. Figure 23 shows the fill factor, power conversion efficiency, and quantum efficiency of the solar cell structure against an X nm ZnS absorber layer thickness. The fill factor, power conversion efficiency, and quantum efficiency were 72.28%, 3.63%, and 48%, respectively, at a 25 nm ZnS absorber layer thickness. At a 50 nm ZnS absorber layer thickness, the fill factor, power conversion efficiency, and quantum efficiency were 78.02%, 11.23%, and 94%, respectively. At a 55 nm ZnS absorber layer thickness, the fill factor, power conversion efficiency, and quantum efficiency were 74.83%, 3.78%, and 52.3%, respectively. The fill factor, power conversion efficiency, and quantum efficiency were 75%, 3.98%, and 53%, respectively, at a 75 nm ZnS absorber layer thickness. The fill factor, power conversion efficiency, and quantum efficiency were 74.82%, 3.8%, and 57.5%, respectively, at a 100 nm ZnS absorber layer thickness.

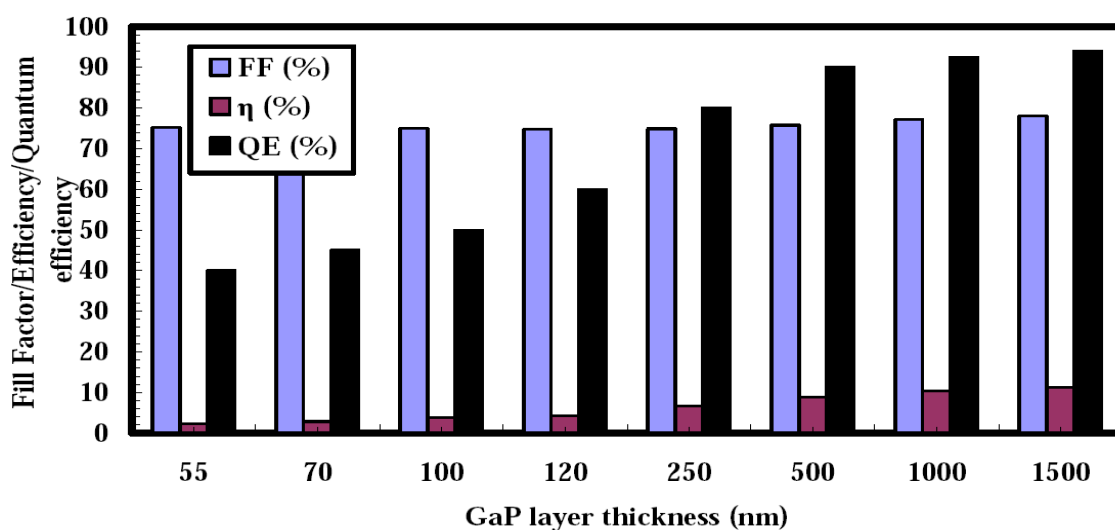


Figure 21. The fill factors, power conversion efficiencies, and quantum efficiencies of the solar cell structure for the various GaP absorber layer thicknesses.

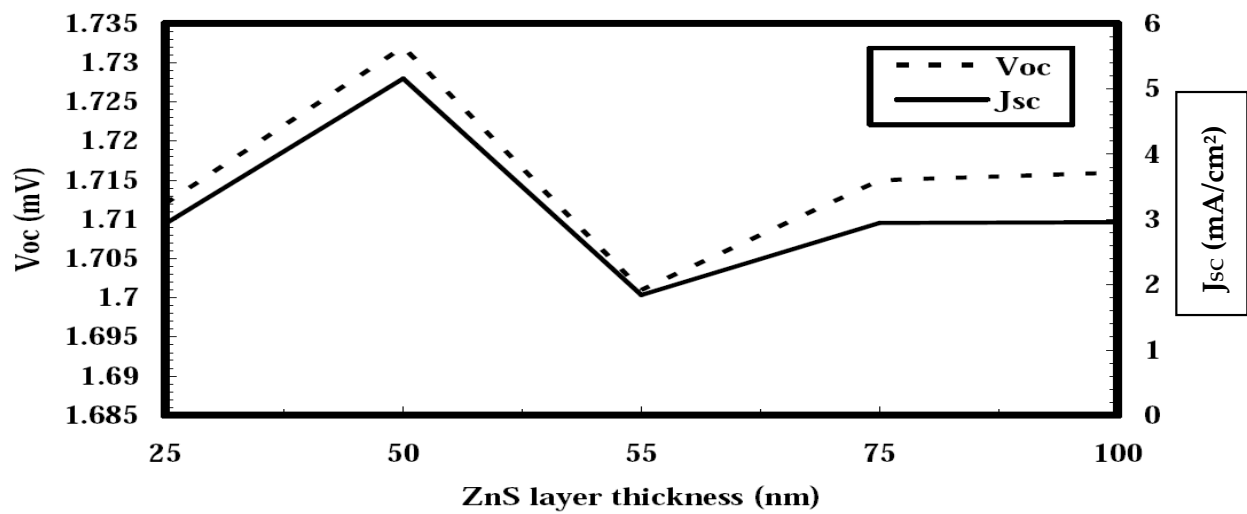


Figure 22. The short-circuit current density/open-circuit voltage of the solar cell structure for the various ZnS absorber layer thicknesses.

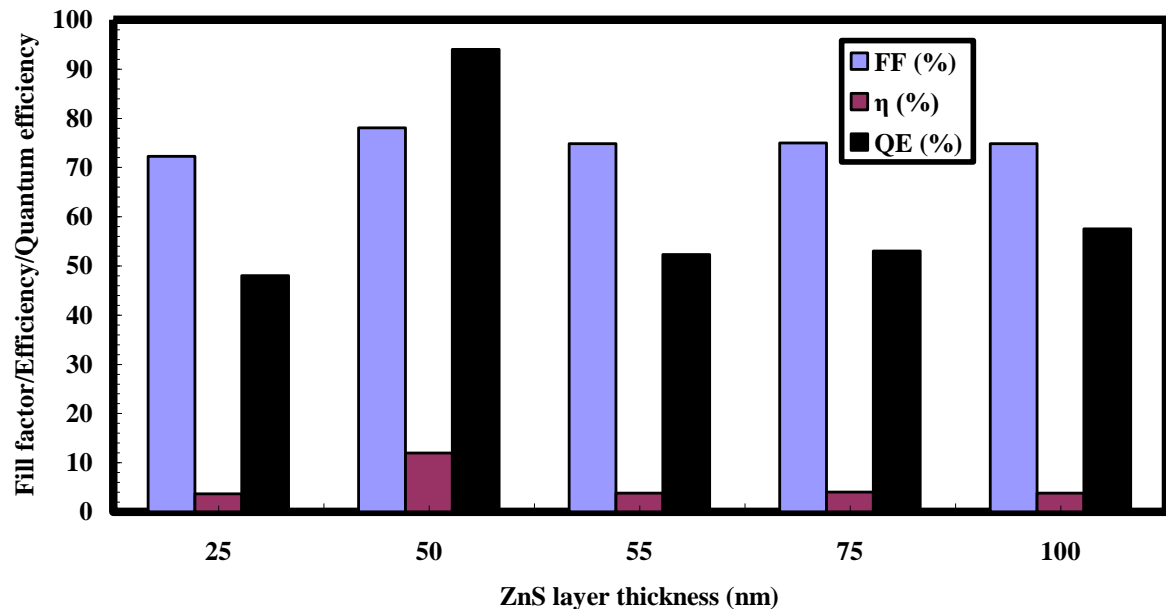


Figure 23. The fill factors, power conversion efficiencies, and quantum efficiencies of the solar cell structure for the various ZnS absorber layer thicknesses.

Figure 24 shows the short-circuit current density/open-circuit voltage of the solar cell structure against the various ZnO:Al absorber layer thicknesses. The open-circuit voltage and the short-circuit current density were 1.714 mV and 2.95 mA/cm<sup>2</sup>, respectively, at a 30 nm ZnO:Al absorber layer thickness. The short-circuit current density and the open-circuit voltage were 5.16 mA/cm<sup>2</sup> and 1.732 mV, respectively, at a 50 nm ZnO:Al absorber layer thickness. The open-circuit voltage and short-circuit current density were 1.72 mV and 3.362 mA/cm<sup>2</sup>, respectively, at a 65 nm ZnO:Al absorber layer thickness. The short-circuit current density and open-circuit voltage were 0.982 mA/cm<sup>2</sup> and 1.714 mV, respectively, at a 100 nm ZnO:Al absorber layer thickness.

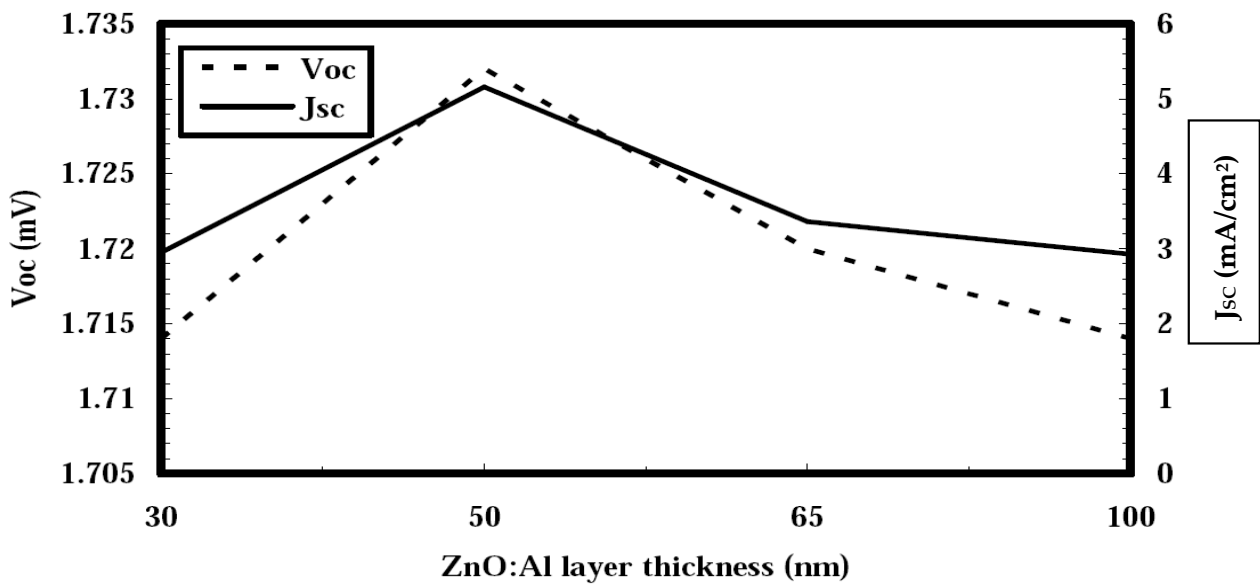


Figure 24. The short-circuit current density and open-circuit voltage of the solar cell structure of the various ZnO:Al absorber layer thicknesses.

Figure 25 clarifies the fill factor, power conversion efficiency, and quantum efficiency of the solar cell structure of the various ZnO:Al absorber layer thicknesses. The fill factor, power conversion efficiency, and quantum efficiency were 74.94%, 3.79%, and 60%, respectively, at a 30 nm ZnO:Al absorber layer thickness. The fill factor, power conversion efficiency, and quantum efficiency were 77.11%, 10.42%, and 92.5%, respectively, at a 50 nm ZnO:Al absorber layer thickness. The fill factor, power conversion efficiency, and quantum efficiency were 74.75%, 4.32%, and 61%, respectively, at a 65 nm ZnO:Al absorber layer thickness. The fill factor, power conversion efficiency, and quantum efficiency were 74.8%, 3.78%, and 49%, respectively, at a 100 nm ZnO:Al absorber layer thickness. The keys for the optimum performance parameters of the suggested and previous solar cell structures are illustrated in Table 2.

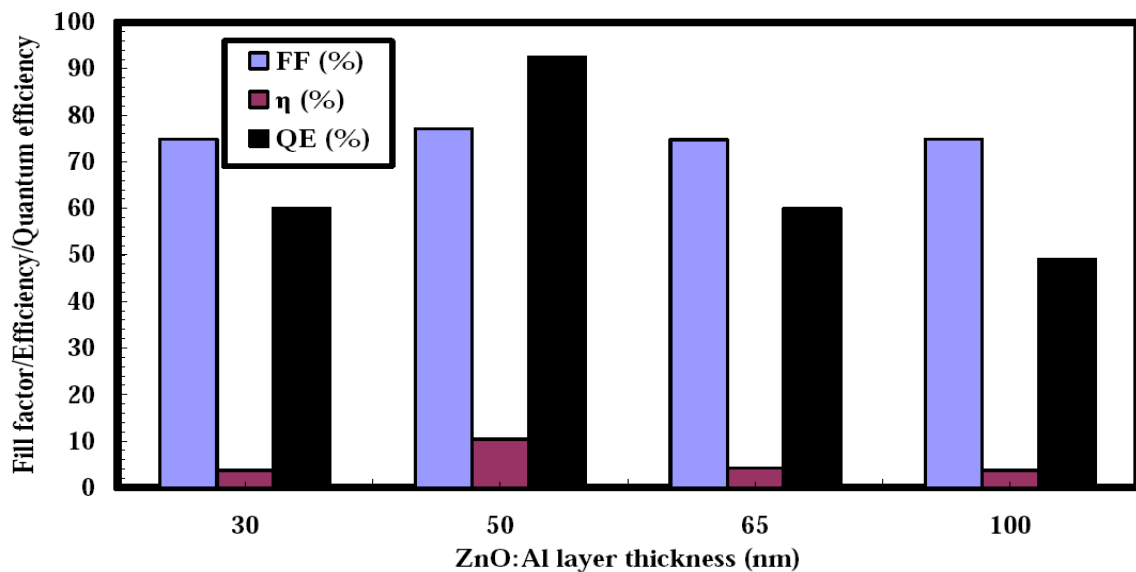


Figure 25. The fill factor, power conversion efficiency, and quantum efficiency of the solar cell structure for the various ZnO:Al absorber layer thicknesses.

The maximum power voltage ( $V_{mp}$ ) was 503.559 mV, the maximum power current ( $J_{mp}$ ) was 48.8075 mA/cm<sup>2</sup>, the short-circuit current ( $J_{sc}$ ) was 51.8738 mA/cm<sup>2</sup>, and the

open-circuit voltage ( $V_{oc}$ ) was 637.552 mV. Table 2 clarifies the comparison of our proposed solar cell structure with previous works.

**Table 2.** Comparison of our proposed solar cell structure with previous works.

	Basic Solar Cell Structure	Solar Cell Circuit Key Parameters			
		$V_{oc}$ (mV)	$J_{sc}$ (mA/cm <sup>2</sup> )	FF (%)	$\eta$ (%)
Ref. [34]	ZnS/CdS/CdTe	740	22.4	62.1	10.3
Ref. [35]	ZnO/CdS/CdTe	1810	7.01	78.84	10
Ref. [36]	Al:ZnO/CdS/CdTe	834	24.7	75.9	15.6
Ref. [37]	ZnO/CdTe	–	–	–	8
Ref. [38]	ZnO/CdS/CdTe	875	21	70.7	12.77
Ref. [39]	ZnO/CdS/CdTe	1000	26.15	76.9	18.3
Ref. [40]	CdTe/CdS/ZnO/Cu	917	28.45	75.99	19.83
Ref. [41]	CdTe/CdS/SnO <sub>2</sub> /FTO	813	27.72	66.03	13.8
This work	SWCNT/CdS/ZnO/Si	637.552	51.8738	74.31	29.91

## 6. Conclusions

The optimized solar cell structure design was clarified against various suitable absorbers, substrates, and contact layer structures. The reflection, absorption, and transmission (RAT) of the solar cell spectrum were simulated versus the spectrum wavelength variations. The effects of the surface morphology were clarified against the photo-current absorptions. The substrate material variation effects were demonstrated against the photo-current absorptions and solar cell quantum efficiencies. The absorber material layer variation effects were studied against the photo-current absorptions. In addition, the contact layer material variation effects were clarified against the photo-current reflections and absorptions of the solar cell. The equivalent circuit modeling and circuit performance parameter optimizations were demonstrated against and compared with other previous studies. A comprehensive research endeavor was conducted that focused on enhancing the efficiency of the proposed solar cell design. The integration of the simulation techniques, judicious material selection, and meticulous performance metrics showcased a methodical approach toward creating a solar cell capable of achieving high efficiency across a wide spectrum of light. Having said this, many researchers are still working on the efficiency potential—based on external radiative efficiency, open-circuit voltage loss, and fill factor loss—of high-efficiency solar cells.

**Author Contributions:** Conceptualization, H.M.E.-H. and A.N.Z.R.; methodology, H.A., software, M.A.A.; validation, M.A.M., A.N.Z.R. and Y.H.A.; formal analysis, H.M.E.-H.; investigation, resources, H.M.E.-H. and A.N.Z.R.; data curation, H.A., M.T.A. and M.A.M.; writing—original draft preparation, H.M.E.-H. and A.N.Z.R.; writing—review and editing, H.A.; visualization, H.M.E.-H. and A.N.Z.R.; supervision, H.M.E.-H. and A.N.Z.R.; project administration, M.A.M. All authors have read and agreed to the published version of the manuscript.

**Funding:** This research was supported by the Deputyship for Research & Innovation, Ministry of Education in Saudi Arabia, as well as by the University of Tabuk (grant number S-1443-0149).

**Data Availability Statement:** Not applicable.

**Acknowledgments:** The authors extend their appreciation to the Deputyship for Research & Innovation, Ministry of Education in Saudi Arabia, for funding this research work through project number S-1443-0149.

**Conflicts of Interest:** The authors declare that they have no conflict of interest to report regarding the present study.

## References

1. Soonmin, H.; Hardani; Nandi, P.; Mwankemwa, B.S.; Malevu, T.D.; Malik, M.I. Overview on Different Types of Solar Cells: An Update. *Appl. Sci.* **2023**, *13*, 2051. [\[CrossRef\]](#)
2. Zalas, M.; Jelak, K. Optimization of platinum precursor concentration for new, fast and simple fabrication method of counter electrode for DSSC application. *Optik Int. J. Light Electron Opt.* **2020**, *206*, 164–175. [\[CrossRef\]](#)
3. Madadi, D. Achieving beyond 26.6% efficiency for graded bandgap perovskite solar cell: Theoretical study. *Mater. Chem. Phys.* **2023**, *308*, 128231. [\[CrossRef\]](#)
4. Prasanna, J.L.; Goel, E.; Kumar, A.; Laref, A.; Santhosh, C.; Ranjan, P.; Kumar, A. Bandgap graded perovskite solar cell for above 30% efficiency. *Optik* **2022**, *269*, 169891. [\[CrossRef\]](#)
5. Siegler, T.D.; Shimpi, T.M.; Sampath, W.S.; Korgel, B.A. Development of wide bandgap perovskites for next-generation low-cost CdTe tandem solar cells. *Chem. Eng. Sci.* **2019**, *199*, 388–397. [\[CrossRef\]](#)
6. Saha, P.; Singh, S.; Bhattacharya, S. Efficient and Lead-Free Perovskite Solar Cells Based on Defect-Ordered Methyl Ammonium Antimony Iodide. *IEEE Trans. Electron Devices* **2023**, *70*, 1095–1101. [\[CrossRef\]](#)
7. Gulomov, J.; Accouche, O. Gold Nanoparticles Introduced ZnO/Perovskite/ Silicon Heterojunction Solar Cell. *IEEE Access* **2022**, *10*, 119558–119565. [\[CrossRef\]](#)
8. Kaifi, M.; Gupta, S.K. Simulation of Perovskite based Solar Cell and Photodetector using SCAPS Software. *Int. J. Eng. Res. Technol.* **2019**, *12*, 1778–1786.
9. Ziani, N.; Belkaid, M.S. Computer Modeling Zinc Oxide/Silicon Heterojunction Solar Cells. *J. Nano-Electron. Phys.* **2018**, *10*, 06002. [\[CrossRef\]](#)
10. Morales-Vilches, A.B.; Cruz, A.; Pingel, S.; Neubert, S.; Mazzarella, L.; Meza, D.; Korte, L.; Schlatmann, R.; Stannowski, B. ITO-Free Silicon Heterojunction Solar Cells with ZnO:Al/SiO<sub>2</sub> Front Electrodes Reaching a Conversion Efficiency of 23%. *IEEE J. Photovoltaics* **2019**, *9*, 34–39. [\[CrossRef\]](#)
11. Pham, D.P.; Lee, S.; Kim, S.; Chowdhury, S.; Khokhar, M.Q.; Le, A.H.T.; Kim, Y.; Park, J.; Yi, J. Wide-gap ZnO layer as electron-selective front contact for single-junction GaAs solar cells. *Mater. Sci. Semicond. Process.* **2021**, *121*, 105344. [\[CrossRef\]](#)
12. Mamta; Singh, Y.; Maurya, K.; Singh, V. n-Si/p-Sb<sub>2</sub>Se<sub>3</sub> structure based simple solar cell device. *Mater. Today Sustain.* **2022**, *18*, 100148. [\[CrossRef\]](#)
13. Ali, Z.; Ali, K.; Hussain, B.; Maqsood, S.; Iqbal, I. Towards the enhanced efficiency of ultrathin Sb<sub>2</sub>Se<sub>3</sub> based solar cell with cubic silicon carbide (3C-SiC) buffer layer. *Opt. Mater.* **2022**, *128*, 112358. [\[CrossRef\]](#)
14. Singh, Y.; Rani, S.; Shashi; Parmar, R.; Kumari, R.; Kumar, M.; Sairam, A.B.; Mamta; Singh, V. Sb<sub>2</sub>Se<sub>3</sub> heterostructure solar cells: Techniques to improve efficiency. *Sol. Energy* **2023**, *249*, 174–182. [\[CrossRef\]](#)
15. Zapukhlyak, Z.R.; Nykyryu, L.I.; Prokopiv, V.V.; Lishchynskyy, I.M.; Katanova, L.O.; Yavorskyi, R.S.; Rubish, V.M.; Wisz, G.; Galushchak, M.O. SCAPS Simulation of ZnO/CdS/CdTe/CuO Heterostructure for Photovoltaic Application. *Phys. Chem. Solid State* **2020**, *21*, 660–668. [\[CrossRef\]](#)
16. Hajjiah, A. COMSOL simulation of non-radiative recombination heat and joule heat in CZTSSe thin film solar cells. *Micro Nanostruct.* **2022**, *168*, 207313. [\[CrossRef\]](#)
17. Zandi, S.; Saxena, P.; Razaghi, M.; Gorji, N.E. Simulation of CZTSSe Thin-Film Solar Cells in COMSOL: Three-Dimensional Optical, Electrical, and Thermal Models. *IEEE J. Photovoltaics* **2020**, *10*, 1503–1507. [\[CrossRef\]](#)
18. Saxena, P.; Gorji, N.E. COMSOL Simulation of Heat Distribution in Perovskite Solar Cells: Coupled Optical–Electrical–Thermal 3-D Analysis. *IEEE J. Photovoltaics* **2019**, *9*, 1693–1698. [\[CrossRef\]](#)
19. Zaky, A.A.; Elewa, S.; Alyahya, S.; Al-Dhaifallah, M.; Rezk, H.; Yousif, B. Mitigation of Temperature Effects and Performance Enhancement of Perovskite Solar Cells Using Nano-Pyramids Grating. *IEEE Access* **2023**, *11*, 36399–36408. [\[CrossRef\]](#)
20. Singh, A.; Ghosh, R.; Agarwal, P. Selection of materials and optimization of antireflection coatings for silicon solar cells using Sentaurus TCAD. *J. Mater. Sci. Mater. Electron.* **2023**, *34*, 1235. [\[CrossRef\]](#)
21. Guo, S.; Ma, F.-J.; Hoex, B.; Aberle, A.G.; Peters, M. Analysing Solar Cells by Circuit Modelling. *Energy Procedia* **2012**, *25*, 28–33. [\[CrossRef\]](#)
22. Gulomov, J.; Aliev, R.; Mirzaalimov, A.; Mirzaalimov, N.; Kakhkhorov, J.; Rashidov, B.; Temirov, S. Studying the Effect of Light Incidence Angle on Photoelectric Parameters of Solar Cells by Simulation. *Int. J. Renew. Energy Dev.* **2021**, *10*, 731–736. [\[CrossRef\]](#)
23. Gulomov, J.; Aliev, R.; Abduvoxidov, M.; Mirzaalimov, A.; Mirzaalimov, N. Exploring optical properties of solar cells by programming and modeling. *Glob. J. Eng. Technol. Adv.* **2020**, *5*, 032–038. [\[CrossRef\]](#)
24. Danladi, E.; Achem, C.U.; Echi, I.O.; Michael, S.U.; Oni, M.E. Thickness Variation Study of Perovskite Layer Over the Range 100–1300 nm and Its Influence on the Performance of Perovskite Solar Cells Using SCAPS Software. *J. Nano Mater. Sci. Res.* **2022**, *1*, 22–27.
25. Eskandari, M.; Rostami, G.; Dolatyari, M.; Rostami, A.; Heidarzadeh, H. Optimization of power conversion efficiency in multi band solar cells (theoretical investigation using GA optimization). *Opt. Quantum Electron.* **2021**, *53*, 469. [\[CrossRef\]](#)
26. Ojha, V.; Jansen, G.; Patanè, A.; La Magna, A.; Romano, V.; Nicosia, G. Design and characterization of effective solar cells. *Energy Syst.* **2022**, *13*, 355–382. [\[CrossRef\]](#)
27. Baniyounis, M.J.; Mohammed, W.F.; Abuhashash, R.T. Analysis of power conversion limitation factors of Cu (In<sub>x</sub>Ga<sub>1-x</sub>) (Se)<sub>2</sub> thin-film solar cells using SCAPS. *Mater. Renew. Sustain. Energy* **2022**, *11*, 215–223. [\[CrossRef\]](#)

28. Balasubrahmanyam, C.S.; Gupta, O.H. Detailed Study of Solar Energy Conversion System using Boost Converter—A New MPPT Technique. *J. Inst. Eng. Ser. B* **2020**, *101*, 631–639. [[CrossRef](#)]
29. Tahhan, S.R.; Taha, R.M. Mercedes Benz logo based plasmon resonance PCF sensor. *Sens. Bio-Sens.* **2021**, *35*, 100468. [[CrossRef](#)]
30. Li, Z.; Ni, M.; Feng, X.D. Simulation of the  $\text{Sb}_2\text{Se}_3$  solar cell with a hole transport layer. *Mater. Res. Express* **2019**, *7*, 16–32.
31. Benami, A. Effect of CZTS Parameters on Photovoltaic Solar Cell from Numerical Simulation. *J. Energy Power Eng.* **2019**, *13*, 32–36. [[CrossRef](#)]
32. Available online: [www.pvlighthouse.com.au](http://www.pvlighthouse.com.au) (accessed on 11 August 2023).
33. Mamta, M.; Maurya, K.K.; Singh, V.N. Enhancing the Performance of an  $\text{Sb}_2\text{Se}_3$ -Based Solar Cell by Dual Buffer Layer. *Sustainability* **2021**, *13*, 12320. [[CrossRef](#)]
34. Han, J.; Fu, G.; Krishnakumar, V.; Liao, C.; Jaegermann, W.; Besland, M. Preparation and characterization of ZnS/CdS bi-layer for CdTe solar cell application. *J. Phys. Chem. Solids* **2013**, *74*, 1879–1883. [[CrossRef](#)]
35. Skhouni, O.; El Manouni, A.; Mari, B.; Ullah, H. Numerical study of the influence of ZnTe thickness on CdS/ZnTe solar cell performance. *Eur. Phys. J. Appl. Phys.* **2016**, *74*, 24602. [[CrossRef](#)]
36. Perrenoud, J.; Kranz, L.; Buecheler, S.; Pianezzi, F.; Tiwari, A.N. The use of aluminum doped ZnO as transparent conductive oxide for CdS/CdTe solar cells. *Thin Solid Film* **2011**, *519*, 7444–7448. [[CrossRef](#)]
37. Aranovich, J.A.; Golmayo, D.; Fahrenbruch, A.L.; Bube, R.H. Photovoltaic properties of ZnO/CdTe heterojunctions prepared by spray pyrolysis. *J. Appl. Phys.* **2012**, *51*, 4260–4268. [[CrossRef](#)]
38. Liu, T.; He, X.; Zhang, J.; Feng, L.; Wu, L.; Li, W.; Zeng, G.; Li, B. Effect of ZnO films on CdTe solar cells. *J. Semicond.* **2012**, *33*, 11–120. [[CrossRef](#)]
39. Matin, M.A.; Amin, N.; Zaharim, A.; Sopian, K. A study towards the possibility of ultra thin CdS/CdTe high efficiency solar cells from numerical analysis. *Wseas Trans. Environ.* **2010**, *6*, 571–580.
40. Fardi, H.; Buny, F. Characterization and Modeling of CdS/CdTe Heterojunction Thin-Film Solar Cell for High Efficiency Performance. *Int. J. Photoenergy* **2013**, *6*, 176–188. [[CrossRef](#)]
41. Amoupour, E.; Hassanzadeh, J.; Ziabari, A.A.; Anaraki, P.A. Numerical simulations of ultrathin CdTe solar cells with a  $\text{ZnxCd}_{1-x}\text{S}$  window layer and a  $\text{Cu}_2\text{O}$  hole transport layer. *J. Comput. Electron.* **2021**, *20*, 2501–2510. [[CrossRef](#)]

**Disclaimer/Publisher’s Note:** The statements, opinions and data contained in all publications are solely those of the individual author(s) and contributor(s) and not of MDPI and/or the editor(s). MDPI and/or the editor(s) disclaim responsibility for any injury to people or property resulting from any ideas, methods, instructions or products referred to in the content.